

# Hyper-reduction methods for accelerating nonlinear finite element simulations: open source implementation and reproducible benchmarks

Axel Larsson<sup>1</sup>, Minji Kim<sup>2</sup>, Chris Vales<sup>3</sup>, Sigrid Adriaenssens<sup>1</sup>, Dylan Matthew Copeland<sup>4</sup>, Youngsoo Choi<sup>4</sup>, Siu Wun Cheung<sup>4\*</sup>

<sup>1</sup>Department of Civil and Environmental Engineering, Princeton University, Princeton, NJ 08540, USA.

<sup>2</sup>Department of Statistics and Operations Research, The University of North Carolina at Chapel Hill, Chapel Hill, NC 27599, USA.

<sup>3</sup>Department of Mathematics, Dartmouth College, Hanover, NH 03755, USA.

<sup>4</sup>Center for Applied Scientific Computing, Lawrence Livermore National Laboratory, Livermore, CA 94550, USA.

\*Corresponding author(s). E-mail(s): [cheung26@llnl.gov](mailto:cheung26@llnl.gov);  
Contributing authors: [a.larsson@princeton.edu](mailto:a.larsson@princeton.edu); [mkim5@unc.edu](mailto:mkim5@unc.edu);  
[chris.vales@dartmouth.edu](mailto:chris.vales@dartmouth.edu); [sadriaen@princeton.edu](mailto:sadriaen@princeton.edu);  
[copeland11@llnl.gov](mailto:copeland11@llnl.gov); [choi15@llnl.gov](mailto:choi15@llnl.gov);

## Abstract

Hyper-reduction methods have gained increasing attention for their potential to accelerate reduced order models for nonlinear systems, yet their comparative accuracy and computational efficiency are not well understood. Motivated by this gap, we evaluate a range of hyper-reduction techniques for nonlinear finite element models across benchmark problems of varying complexity, assessing the inevitable tradeoff between accuracy and speedup. More specifically, we consider interpolation methods based on the gappy proper orthogonal decomposition as well as the empirical quadrature procedure (EQP), and apply them to the hyper-reduction of problems in nonlinear diffusion, nonlinear elasticity and Lagrangian hydrodynamics. Our numerical results are generated using the open source `libROM`, `Laghos` and `MFEM` numerical libraries. Our findings reveal that the comparative performance between hyper-reduction methods depends on both the problem and the choice of time integration method. The EQP method generally

achieves lower relative errors than interpolation methods and is more efficient in terms of quadrature point usage, resulting in a lower wall time for the non-linear diffusion and elasticity problems. However, its online computational cost is observed to be relatively high for Lagrangian hydrodynamics problems. Conversely, interpolation methods exhibit greater variability, especially with respect to the use of different time integration methods in the Lagrangian hydrodynamics problems. The presented results underscore the need for problem specific method selection to balance accuracy and efficiency, while also offering useful guidance for future comparisons and refinements of hyper-reduction techniques.

**Keywords:** model reduction, projection based reduction, hyper-reduction, finite element method, open source software

## 1 Introduction

Partial differential equations (PDEs) are employed in numerous scientific fields to model the behavior of spatiotemporal systems. Despite their vast utility, only a few PDEs of practical interest have known analytical solutions under general conditions. As such, in most applications approximate PDE solutions are sought by various discretization methods, such as the finite differences method or the finite element method (FEM). In this study we consider the spatial discretization of time-dependent PDEs with algebraic constraints, resulting in systems of semi-explicit differential-algebraic equations (DAEs)

$$\begin{aligned} \mathbf{M} \frac{d\mathbf{y}}{dt} + \mathbf{A}\mathbf{y} + \mathbf{B}\mathbf{z} &= \mathbf{f}(\mathbf{y}, \mathbf{z}, t) \\ \mathbf{B}^\top \mathbf{y} + \mathbf{C}\mathbf{z} &= \mathbf{g}(\mathbf{y}, \mathbf{z}, t) \\ \mathbf{y}(0) &= \mathbf{y}_0 \end{aligned} \tag{1}$$

where  $t \in [0, T]$  denotes time,  $\mathbf{y} \in [0, T] \rightarrow \mathbb{R}^{N_y}$  is the differential variable with a prescribed initial condition  $\mathbf{y}_0 \in \mathbb{R}^{N_y}$  and  $\mathbf{z} \in [0, T] \rightarrow \mathbb{R}^{N_z}$  is the algebraic variable. Moreover,  $\mathbf{M} \in \mathbb{R}^{N_y \times N_y}$  is the system mass matrix,  $\mathbf{A} \in \mathbb{R}^{N_y \times N_y}$ ,  $\mathbf{C} \in \mathbb{R}^{N_z \times N_z}$  are linear operator matrices, and  $\mathbf{B} \in \mathbb{R}^{N_y \times N_z}$  is a constraint matrix. Finally,  $\mathbf{f} : \mathbb{R}^{N_y} \times \mathbb{R}^{N_z} \times (0, T) \rightarrow \mathbb{R}^{N_y}$  and  $\mathbf{g} : \mathbb{R}^{N_y} \times \mathbb{R}^{N_z} \times (0, T) \rightarrow \mathbb{R}^{N_z}$  are nonlinear functions.

Time integration schemes such as multistep and Runge-Kutta methods can be used to solve the ODE part of the semi-explicit DAE system in (1), with  $\mathbf{z}$  solved algebraically. However, for many important physical systems the associated PDEs are nonlinear and require a fine mesh to resolve the solution, rendering the numerical modeling of such systems computationally expensive. This expense is compounded in multi-query applications such as PDE-constrained optimization [1–4] where a large number of repeated PDE solves are necessary. For instance, design optimization of inertial confinement fusion experiments requires the determination of more than a dozen independent parameters. Depending on the fidelity of the physics model, each forward simulation takes a few minutes to hundreds of CPU hours to complete [5]. When

employing a simple gradient based optimization algorithm, finite difference approximation of the objective function gradient requires as many radiation hydrodynamics simulations as the dimension of the parameter search space, resulting in prohibitively high computational cost for every parameter update.

For these reasons, it is of great interest to develop methodologies that accelerate the solving of large scale nonlinear PDEs. One such methodology is reduced order modeling, where a full order model (FOM) is approximated with an accurate but computationally inexpensive reduced order model (ROM). ROMs can be divided into two main classes: data based and physics based. Purely data based methods such as dynamic mode decomposition (DMD) [6, 7] or neural network approximation [8, 9] have the benefit of not requiring prior knowledge of the PDE problem specification. However, they typically do not make accurate predictions in extrapolation and are not robust to noisy input data [10]. On the other hand, physics based ROM approaches incorporate prior knowledge into the ROM formulation and typically fare better in terms of generalization than purely data based approaches [10]. Physics based ROM approaches include physics informed neural networks [11], neural operators [12] and projection-based reduced order models (pROMs), which are the class of ROMs studied in this paper. At a high level, a pROM projects the PDE onto a low dimensional subspace which approximates the PDE solution space. The projected PDE is then solved in subspace coordinates, leading to reduced computational cost. For a more comprehensive description of pROMs we refer the reader to the survey papers [13, 14].

Projection based ROMs have been shown to efficiently accelerate the solving of physics problems such as the Burgers equation [15–18], the Navier-Stokes equations [19, 20], nonlinear diffusion problems [21, 22], convection-diffusion problems [23], the shallow water equations [24, 25], the Euler equations [26–28], wave problems [29, 30], Boltzmann transport problems [31] and the Schrödinger equation [32]. In addition, pROMs can enable substantial speed-up in design optimization problems such as lattice structure design [33], flutter avoidance wing shape optimization [34], topology optimization of wind turbine blades [35], reservoir simulations [36–38] and rocket nozzle shape design [39].

In the standard pROM formulation, the effects of the nonlinear terms  $\mathbf{f}$  and  $\mathbf{g}$  in the ROM subspaces are evaluated on the FOM mesh. This causes the pROM computational cost to scale with the FOM size, significantly reducing their efficiency. Hyper-reduction methods address this issue by approximating the nonlinear terms through evaluation at a reduced set of sample points, thereby achieving substantial computational speedup while maintaining a low approximation error. As indicated in [40], hyper-reduction methods can be broadly classified into two categories. The first category consists of interpolation or “approximate-then-project” methods, which interpolate the nonlinear terms at a subset of selected nodes before projecting them onto the reduced-order basis (ROB). This class of methods originates in the gappy proper orthogonal decomposition (POD) approach [41], which reconstructs high dimensional data using empirical basis functions. These methods rely on interpolation based approximations, where different sampling methods [42–47] are introduced to select interpolation points for optimizing the tradeoff between accuracy and speedup. The second category comprises quadrature or “project-then-approximate” methods, which

directly approximate the reduced nonlinear terms by constructing sparse quadrature rules. These methods can be viewed as data based quadrature techniques, where both the sample points and associated weights are optimized using training data. Examples include the seminal work by An et al. [48], the energy-conserving sampling and weighting method [49], the empirical cubature method [50] and the empirical quadrature procedure (EQP) [51, 52].

Given that hyper-reduction methods are being employed in applications across various domains, a comprehensive comparative analysis of their accuracy and efficiency is of significant interest. Existing works have provided valuable insights into specific hyper-reduction techniques, with recent efforts focusing on a single application at a time, such as nonlinear heat conduction [22, 53], magneto-mechanics [54, 55] and the Navier-Stokes equations [56].

In the present study we undertake a detailed empirical comparison of several hyper-reduction methods by applying them to a diverse selection of problem cases. More specifically, we consider DEIM [43, 44], Q-DEIM [45] and S-OPT [47] from the class of interpolation methods and EQP [52] from the class of quadrature methods. We apply these methods to three distinct and challenging nonlinear benchmark problems discretized by finite element methods: nonlinear heat conduction, nonlinear elasticity and Lagrangian hydrodynamics. The main features of our work can be summarized as follows.

1. *Comparison.* We present a broad comparison of hyper-reduction methods, including both interpolation and quadrature methods.
2. *Application.* We evaluate each considered hyper-reduction method on three application domains with distinct challenges, revealing tradeoffs between accuracy and computational speedup.
3. *Open source implementation.* We employ an open source numerical implementation of all hyper-reduction methods and problem cases considered in this work, using the `libROM` [57], `Laghos` [58] and `MFEM` [59] numerical libraries and providing the commands that can be used for their reproduction.

The remainder of the paper is structured as follows. Section 2 introduces a unified variational framework to describe the example problems and discusses their finite element discretization. Section 3 serves as an introduction to the pROM approach used for the linear part of the ROM formulation. Section 4 presents the different hyper-reduction methods compared in this work, which are used to approximate the evaluation of nonlinear terms. Section 5 describes the example problems and presents our numerical results, followed by a discussion in Section 6. Finally, Appendix A provides details on how to reproduce our numerical results.

## 2 Finite element discretization

Considering (1) in a variational setting we seek  $y \in L^2(0, T; \mathcal{Y})$  and  $z \in L^2(0, T; \mathcal{Z})$  such that  $dy/dt \in L^2(0, T; \mathcal{Y}')$ , where  $\mathcal{H}$  and  $\mathcal{Z}$  are Hilbert spaces and  $\mathcal{Y} \subset \mathcal{H} \subset \mathcal{Y}'$  forms a Gelfand triple (rigged Hilbert space). In addition, we ask that the following

equations be satisfied for any  $\varphi \in \mathcal{Y}$  and  $\lambda \in \mathcal{Z}$

$$\begin{aligned} \frac{d}{dt}(y(t), \varphi)_{\mathcal{H}} + a(y(t), \varphi) + b(\varphi, z(t)) &= \langle f(y, z, t), \varphi \rangle_{\mathcal{Y}' \times \mathcal{Y}} \\ b(y(t), \lambda) + c(z(t), \lambda) &= \langle g(y, z, t), \lambda \rangle_{\mathcal{Z}' \times \mathcal{Z}} \end{aligned} \quad (2)$$

where  $\langle \cdot, \cdot \rangle_{\mathcal{Y}' \times \mathcal{Y}}$  denotes the duality pairing between  $\mathcal{Y}'$  and  $\mathcal{Y}$  and  $(\cdot, \cdot)_{\mathcal{H}}$  the scalar product on  $\mathcal{H}$ . Additionally,  $a : \mathcal{Y} \times \mathcal{Y} \rightarrow \mathbb{R}$ ,  $b : \mathcal{Y} \times \mathcal{Z} \rightarrow \mathbb{R}$  and  $c : \mathcal{Z} \times \mathcal{Z} \rightarrow \mathbb{R}$  denote bilinear forms, while  $f : \mathcal{Y} \times \mathcal{Z} \times (0, T) \rightarrow \mathcal{Y}'$  and  $g : \mathcal{Y} \times \mathcal{Z} \times (0, T) \rightarrow \mathcal{Z}'$  are general nonlinear functions.

The spatial discretization of (2) is carried out using the finite element method, the result of which is the system of differential-algebraic equations presented in (1). To that end, let  $\mathcal{B}_{\mathcal{Y}} = \{\varphi_j\}_{j=1}^{N_y}$  be a basis for a  $\mathcal{Y}$ -conforming finite element space  $\mathcal{Y}^h$ , with  $L_{\mathcal{B}_{\mathcal{Y}}} : \mathcal{Y}^h \rightarrow \mathbb{R}^{N_y}$  the coordinate representation of  $\mathcal{Y}^h$  with respect to  $\mathcal{B}_{\mathcal{Y}}$ . We denote the finite element approximation  $y_h \in \mathcal{Y}^h$  of  $y$  by

$$y_h(t) = \sum_{j=1}^{N_y} \mathbf{y}_j(t) \varphi_j.$$

Similarly, for the algebraic variables let  $\mathcal{B}_{\mathcal{Z}} = \{\lambda_j\}_{j=1}^{N_z}$  be a basis for a  $\mathcal{Z}$ -conforming finite element space  $\mathcal{Z}^h$ , with  $L_{\mathcal{B}_{\mathcal{Z}}} : \mathcal{Z}^h \rightarrow \mathbb{R}^{N_z}$  the coordinate representation of  $\mathcal{Z}^h$  with respect to  $\mathcal{B}_{\mathcal{Z}}$ . The finite element approximation  $z_h \in \mathcal{Z}^h$  of  $z$  is denoted by

$$z_h(t) = \sum_{j=1}^{N_z} \mathbf{z}_j(t) \lambda_j.$$

Then the differential variable vector  $\mathbf{y} = L_{\mathcal{B}_{\mathcal{Y}}}(y_h) : [0, T] \rightarrow \mathbb{R}^{N_y}$  and the algebraic variable vector  $\mathbf{z} = L_{\mathcal{B}_{\mathcal{Z}}}(z_h) : [0, T] \rightarrow \mathbb{R}^{N_z}$  satisfy (1), where the vector and matrix representations are defined entrywise by

$$\begin{aligned} \mathbf{M}_{j,j'} &= (\varphi_{j'}, \varphi_j)_{\mathcal{H}} & \mathbf{A}_{j,j'} &= a(\varphi_{j'}, \varphi_j) \\ \mathbf{B}_{j,j'} &= b(\varphi_{j'}, \lambda_j) & \mathbf{C}_{j,j'} &= c(\lambda_{j'}, \lambda_j) \end{aligned} \quad (3)$$

and

$$\begin{aligned} \mathbf{f}_j(\mathbf{y}, \mathbf{z}, t) &= \left\langle f \left( L_{\mathcal{B}_{\mathcal{Y}}}^{-1}(\mathbf{y}), L_{\mathcal{B}_{\mathcal{Z}}}^{-1}(\mathbf{z}), t \right), \varphi_j \right\rangle_{\mathcal{Y}' \times \mathcal{Y}} \\ \mathbf{g}_j(\mathbf{y}, \mathbf{z}, t) &= \left\langle g \left( L_{\mathcal{B}_{\mathcal{Y}}}^{-1}(\mathbf{y}), L_{\mathcal{B}_{\mathcal{Z}}}^{-1}(\mathbf{z}), t \right), \lambda_j \right\rangle_{\mathcal{Z}' \times \mathcal{Z}}. \end{aligned} \quad (4)$$

### 3 Projection based reduction

As mentioned in Section 1, solving (1) can be computationally expensive when the FOM dimension  $N_y + N_z$  is very large. In such cases, the solution procedure can be

accelerated by projecting the PDE to the affine subspaces  $y_{\text{offset}} + \mathcal{Y}^r$  and  $z_{\text{offset}} + \mathcal{Z}^r$  for the differential and algebraic variables respectively, where

$$\begin{aligned}\dim(\mathcal{Y}^r) &= r_y \ll N_y = \dim(\mathcal{Y}^h) \\ \dim(\mathcal{Z}^r) &= r_z \ll N_z = \dim(\mathcal{Z}^h)\end{aligned}\tag{5}$$

with  $y_{\text{offset}} \in \mathcal{Y}^h$  and  $z_{\text{offset}} \in \mathcal{Z}^h$  denoting the prescribed offsets. The subspaces  $\mathcal{Y}^r$  and  $\mathcal{Z}^r$  are spanned by the sets of basis vectors  $\{\psi_j\}_{j=1}^{r_y} \subset \mathcal{Y}^h$  and  $\{\theta_j\}_{j=1}^{r_z} \subset \mathcal{Z}^h$  respectively

$$\begin{aligned}\mathcal{Y}^r &= \text{span}\{\psi_j\}_{j=1}^{r_y} \subseteq \mathcal{Y}^h \\ \mathcal{Z}^r &= \text{span}\{\theta_j\}_{j=1}^{r_z} \subseteq \mathcal{Z}^h.\end{aligned}\tag{6}$$

The differential and algebraic state vector are then approximated using the subspace basis vectors

$$\begin{aligned}y(t) &\approx \tilde{y}(t) = y_{\text{offset}} + \sum_{j=1}^{r_y} \hat{y}_j(t) \psi_j \\ z(t) &\approx \tilde{z}(t) = z_{\text{offset}} + \sum_{j=1}^{r_z} \hat{z}_j(t) \theta_j.\end{aligned}\tag{7}$$

The reduced system of DAEs is derived by performing the Galerkin projection of (1) onto the introduced subspaces. To that end, we begin by denoting by

$$\hat{\mathbf{y}} = (\hat{y}_1, \dots, \hat{y}_{r_y})^\top : (0, T] \rightarrow \mathbb{R}^{r_y} \quad \hat{\mathbf{z}} = (\hat{z}_1, \dots, \hat{z}_{r_z})^\top : (0, T] \rightarrow \mathbb{R}^{r_z}$$

the vectors of generalized coordinates of the differential and algebraic variables respectively, and by

$$\mathbf{y}_{\text{offset}} = L_{\mathcal{B}_y}(y_{\text{offset}}) \in \mathbb{R}^{N_y} \quad \mathbf{z}_{\text{offset}} = L_{\mathcal{B}_z}(z_{\text{offset}}) \in \mathbb{R}^{N_z}$$

their associated offset vectors. Next, we define the corresponding basis vectors

$$\boldsymbol{\psi}_j = L_{\mathcal{B}_y}(\psi_j) \in \mathbb{R}^{N_y} \quad \boldsymbol{\theta}_j = L_{\mathcal{B}_z}(\theta_j) \in \mathbb{R}^{N_z}$$

and assemble the basis matrices by

$$\boldsymbol{\Psi} = [\boldsymbol{\psi}_1, \boldsymbol{\psi}_2, \dots, \boldsymbol{\psi}_{r_y}] \in \mathbb{R}^{N_y \times r_y} \quad \boldsymbol{\Theta} = [\boldsymbol{\theta}_1, \boldsymbol{\theta}_2, \dots, \boldsymbol{\theta}_{r_z}] \in \mathbb{R}^{N_z \times r_z}.$$

satisfying the orthonormality conditions  $\boldsymbol{\Psi}^\top \boldsymbol{\Psi} = \mathbf{I}_{r_y}$  and  $\boldsymbol{\Theta}^\top \boldsymbol{\Theta} = \mathbf{I}_{r_z}$ . With these definitions in place, the approximate variables (7) can be written in vector notation

$$\begin{aligned}\mathbf{y}(t) &\approx \tilde{\mathbf{y}}(t) = \mathbf{y}_{\text{offset}} + \boldsymbol{\Psi} \hat{\mathbf{y}}(t) \\ \mathbf{z}(t) &\approx \tilde{\mathbf{z}}(t) = \mathbf{z}_{\text{offset}} + \boldsymbol{\Theta} \hat{\mathbf{z}}(t).\end{aligned}\tag{8}$$

Invoking the approximation (8) and applying Galerkin projection directly to (1), we obtain the reduced order model of dimension  $r_y + r_z$

$$\begin{aligned}\hat{\mathbf{M}} \frac{d\hat{\mathbf{y}}}{dt} + \hat{\mathbf{A}}\hat{\mathbf{y}} + \hat{\mathbf{B}}\hat{\mathbf{z}} &= \bar{\mathbf{f}}(\mathbf{y}_{\text{offset}} + \Psi\hat{\mathbf{y}}, \mathbf{z}_{\text{offset}} + \Theta\hat{\mathbf{z}}, t) \\ \hat{\mathbf{B}}^\top \hat{\mathbf{y}} + \hat{\mathbf{C}}\hat{\mathbf{z}} &= \bar{\mathbf{g}}(\mathbf{y}_{\text{offset}} + \Psi\hat{\mathbf{y}}, \mathbf{z}_{\text{offset}} + \Theta\hat{\mathbf{z}}, t)\end{aligned}\quad (9)$$

with

$$\begin{aligned}\hat{\mathbf{M}} &= \Psi^\top \mathbf{M} \Psi \in \mathbb{R}^{r_y \times r_y} & \hat{\mathbf{A}} &= \Psi^\top \mathbf{A} \Psi \in \mathbb{R}^{r_y \times r_y} \\ \hat{\mathbf{B}} &= \Psi^\top \mathbf{B} \Theta \in \mathbb{R}^{r_y \times r_z} & \hat{\mathbf{C}} &= \Theta^\top \mathbf{C} \Theta \in \mathbb{R}^{r_z \times r_z}\end{aligned}\quad (10)$$

and

$$\bar{\mathbf{f}} = \Psi^\top \mathbf{f} \in \mathbb{R}^{r_y} \quad \bar{\mathbf{g}} = \Theta^\top \mathbf{g} \in \mathbb{R}^{r_z}. \quad (11)$$

Note that the nonlinear terms  $\bar{\mathbf{f}} : \mathbb{R}^{N_y} \times \mathbb{R}^{N_z} \times \mathbb{R} \rightarrow \mathbb{R}^{r_y}$  and  $\bar{\mathbf{g}} : \mathbb{R}^{N_y} \times \mathbb{R}^{N_z} \times \mathbb{R} \rightarrow \mathbb{R}^{r_z}$  are the orthogonal projections of the image of the vector valued functions  $\mathbf{f}$  and  $\mathbf{g}$  onto the column spaces of  $\Psi$  and  $\Theta$  respectively. The projected functions are defined entrywise as

$$\begin{aligned}\bar{f}_j(\tilde{\mathbf{y}}, \tilde{\mathbf{z}}, t) &= \left\langle f \left( L_{\mathcal{B}_y}^{-1}(\tilde{\mathbf{y}}), L_{\mathcal{B}_z}^{-1}(\tilde{\mathbf{z}}), t \right), \psi_j \right\rangle_{\mathcal{Y}' \times \mathcal{Y}} \\ \bar{g}_j(\tilde{\mathbf{y}}, \tilde{\mathbf{z}}, t) &= \left\langle g \left( L_{\mathcal{B}_y}^{-1}(\tilde{\mathbf{y}}), L_{\mathcal{B}_z}^{-1}(\tilde{\mathbf{z}}), t \right), \theta_j \right\rangle_{\mathcal{Z}' \times \mathcal{Z}}\end{aligned}\quad (12)$$

which involves integration of the shown integrand functions over the spatial domain.

The nonlinear terms  $\bar{\mathbf{f}}$  and  $\bar{\mathbf{g}}$  defined in (12) are evaluated on the FOM-size vectors  $\tilde{\mathbf{y}} \in N_y$  and  $\tilde{\mathbf{z}} \in N_z$  respectively. Given that the FOM size parameters  $N_y \gg r_y$  and  $N_z \gg r_z$  are generally significantly larger than the reduced ones  $r_y$  and  $r_z$ , the evaluation of the nonlinear terms  $\bar{\mathbf{f}}$  and  $\bar{\mathbf{g}}$  is expected to dominate the ROM computational cost and prevent it from achieving significant speedup. To overcome this issue, the evaluation of  $\bar{\mathbf{f}}$  and  $\bar{\mathbf{g}}$  is approximated by sampling  $\mathbf{f}$  and  $\mathbf{g}$  at a small number of evaluation points, giving rise to various hyper-reduction methods.

In the next section we focus on hyper-reduction methods that are based on interpolation or quadrature, presenting their formulation and computational implementation.

## 4 Hyper-reduction

As explained in the previous section, the projection based reduction of a nonlinear problems leads to nonlinear terms that retain their dependence on the FOM size parameters  $N_y \gg r_y$  and  $N_z \gg r_z$ . To remove this dependence, various hyper-reduction methods have been developed that approximate the evaluation of the nonlinear terms  $\bar{\mathbf{f}}$  and  $\bar{\mathbf{g}}$ .

In this section we focus on hyper-reduction methods based on interpolation and quadrature techniques. We begin with interpolation techniques, particularly the gappy POD-based family of methods (Section 4.1), where  $\bar{\mathbf{f}}$  and  $\bar{\mathbf{g}}$  are approximated by applying an oblique projection formed by a chosen sampling procedure. We consider three sampling algorithms: DEIM (Section 4.1.1), Q-DEIM (Section 4.1.2) and S-OPT (Section 4.1.3).

We then move on to quadrature techniques and focus on the empirical quadrature procedure (EQP) (Section 4.2). As shown in (12), the nonlinear terms  $\bar{\mathbf{f}}$  and  $\bar{\mathbf{g}}$  are defined as projections of the vector valued functions  $\mathbf{f}$  and  $\mathbf{g}$  onto the derived reduced subspaces. The duality pairings that appear in (12) correspond to integration of the nonlinear integrands over the problem's spatial domain. Based on that, the EQP method derives sparse approximate quadrature rules for  $\bar{\mathbf{f}}$  and  $\bar{\mathbf{g}}$  to approximate their evaluation with reduced cost. In what follows, we focus on the hyper-reduction of  $\bar{\mathbf{f}}$ ; the hyper-reduction of  $\bar{\mathbf{g}}$  can be performed analogously.

#### 4.1 Interpolation methods

Interpolation methods based on the gappy POD hyper-reduction framework [41] construct a reduced basis approximation of  $\mathbf{f}$

$$\mathbf{f}(\tilde{\mathbf{y}}, \tilde{\mathbf{z}}, t) \approx \Xi \hat{\mathbf{f}}(\tilde{\mathbf{y}}, \tilde{\mathbf{z}}, t) \quad (13)$$

where

$$\Xi = [\xi_1 \cdots \xi_{r_f}] \in \mathbb{R}^{N_y \times r_f} \quad r_f \ll N_y$$

is an orthonormal basis matrix whose columns span a reduced subspace of the range of  $\mathbf{f}$ , and  $\hat{\mathbf{f}} \in \mathbb{R}^{r_f}$  denotes the coordinates of  $\mathbf{f}$  with respect to  $\Xi$ . The approximation (13) is performed by interpolation of  $\mathbf{f}$  at  $n_f$  sampled indices, with  $r_f \leq n_f \ll N_y$ . More precisely, let  $\mathcal{Z} = \{i_1, \dots, i_{n_f}\} \subset \{1, \dots, N_y\}$  be a set of sampled indices and  $\mathbf{Z} \in \mathbb{R}^{N_y \times n_f}$  the associated sampling matrix whose entries are given by  $\mathbf{Z}_{j,k} = \delta_{j,i_k}$ . Using the above we formulate a least squares problem for the coordinates

$$\hat{\mathbf{f}} = \arg \min_{\mathbf{c} \in \mathbb{R}^{r_f}} \|\mathbf{Z}^\top (\mathbf{f}(\tilde{\mathbf{y}}, \tilde{\mathbf{z}}, t) - \Xi \mathbf{c})\|_2^2$$

whose solution is given by

$$\hat{\mathbf{f}} = (\mathbf{Z}^\top \Xi)^+ \mathbf{Z}^\top \mathbf{f}(\tilde{\mathbf{y}}, \tilde{\mathbf{z}}, t)$$

where superscript  $+$  denotes the Moore-Penrose pseudoinverse. Inserted to (13), the above solution yields

$$\mathbf{f}(\tilde{\mathbf{y}}, \tilde{\mathbf{z}}, t) \approx \Xi (\mathbf{Z}^\top \Xi)^+ \mathbf{Z}^\top \mathbf{f}(\tilde{\mathbf{y}}, \tilde{\mathbf{z}}, t) = \mathbf{P} \mathbf{f}(\tilde{\mathbf{y}}, \tilde{\mathbf{z}}, t) \quad (14)$$

where matrix  $\mathbf{P} \in \mathbb{R}^{N_y \times N_y}$  defines a rank- $r_f$  oblique projection onto the column space of  $\Xi$ .

Computing the matrix multiplication  $\mathbf{P}\mathbf{f}$  is more computationally expensive than evaluating  $\mathbf{f}$  itself. To reduce the computational cost, we instead compute the product  $\mathbf{Z}^\top \mathbf{f}(\tilde{\mathbf{y}}, \tilde{\mathbf{z}}, t)$  by only evaluating  $\mathbf{f}$  at the sampling indices  $\mathcal{Z}$ . It follows that the selection of sampling indices  $\mathcal{Z}$  affects the oblique projection error  $\|\mathbf{f} - \mathbf{P}\mathbf{f}\|_2$ . An error bound for interpolation methods as a function of  $\mathbf{Z}$  is given in [47, Theorem 3.1]

$$\text{err}(\mathbf{Z}) = \|(\mathbf{I}_N - \mathbf{P})\mathbf{f}\|_2 \leq \|(\mathbf{Z}^\top \Xi)^+\|_2 \|(\mathbf{I}_N - \Xi \Xi^\top)\mathbf{f}\|_2 \quad (15)$$

---

**Algorithm 1** Oversampled DEIM sampling algorithm

---

Input: Basis matrix  $\Xi \in \mathbb{R}^{N \times r_f}$  and desired number of sampled indices  $n_f > r_f$ Output: Set of  $n_f$  sampling indices  $\mathcal{Z} = \{i_1, \dots, i_{n_f}\}$ 

```
 $i_1 = \operatorname{argmax}_i |\Xi_{i,1}|$ 
 $\mathcal{Z} = \{i_1\}$ 
 $n_{\text{iter}} = \operatorname{ceil}(\frac{n_f-1}{r_f-1})$ 
for  $j = 2 : r_f$  do
  Construct  $\Xi^{(j-1)} = \Xi[\mathbf{e}_1, \dots, \mathbf{e}_{j-1}]$ 
  for  $\ell = (j-2)n_{\text{iter}} + 1 : (j-1)n_{\text{iter}}$  do
    Construct  $\mathbf{Z} = [\mathbf{e}_{i_1}, \dots, \mathbf{e}_{i_\ell}]$ 
    Compute  $\boldsymbol{\varepsilon} = \Xi^{(j-1)}(\mathbf{Z}^\top \Xi^{(j-1)})^+ \mathbf{Z}^\top \boldsymbol{\xi}_j$ 
     $i_{\ell+1} = \operatorname{argmax}_i |\Xi_{i,j} - \boldsymbol{\varepsilon}_i|$ 
     $\mathcal{Z} \leftarrow \mathcal{Z} \cup \{i_{\ell+1}\}$ 
  if  $|\mathcal{Z}| = n_f$  then return
  end for
end for
end for
```

---

where the 2-norm  $\|(\mathbf{Z}^\top \Xi)^+\|_2$  is equal to the largest singular value of  $(\mathbf{Z}^\top \Xi)^+$ , or equivalently the reciprocal of the smallest strictly positive singular value of  $\mathbf{Z}^\top \Xi$ . The same theorem provides the alternative expression

$$\|(\mathbf{I}_N - \mathbf{P})\mathbf{f}\|_2^2 = \|(\mathbf{I}_N - \Xi \Xi^\top)\mathbf{f}\|_2^2 + \|\boldsymbol{\varepsilon}(\mathbf{f}, \mathcal{Z})\|_2^2 \quad (16)$$

where  $\boldsymbol{\varepsilon}(\mathbf{f}, \mathcal{Z}) \in \mathbb{R}^{r_f}$  is given by

$$\boldsymbol{\varepsilon}(\mathbf{f}, \mathcal{Z}) = \left( (\mathbf{Z}^\top \Xi)^\top \mathbf{Z}^\top \Xi \right)^{-1} (\mathbf{Z}^\top \Xi)^\top \mathbf{Z}^\top (\mathbf{I}_N - \Xi \Xi^\top) \mathbf{f}. \quad (17)$$

Different strategies for minimizing the error  $\operatorname{err}(\mathbf{Z})$  can be devised based on the expressions (15)-(17), three of which are considered in this work. DEIM sampling methods (Section 4.1.1) aim to lower the error bound in (15) by minimizing the 2-norm of  $(\mathbf{Z}^\top \Xi)^+$ . Q-DEIM sampling methods (Section 4.1.2) have the similar goal of minimizing the condition number of  $(\mathbf{Z}^\top \Xi)^+$  to minimize the error bound. Finally, the S-OPT sampling algorithm (Section 4.1.3) aims first to increase the nonsingularity of  $(\mathbf{Z}^\top \Xi)^\top \mathbf{Z}^\top \Xi$  to increase numerical stability, and second to increase the column orthogonality of  $\mathbf{Z}^\top \Xi$  in order to decrease the 2-norm of  $\boldsymbol{\varepsilon}(\mathbf{f}, \mathcal{Z})$ .

---

**Algorithm 2** GappyPOD+E sampling algorithm

---

Input: Basis matrix  $\Xi \in \mathbb{R}^{N \times r_f}$  and desired number of sampled indices  $n_f$

Output: Set of  $n_f$  sampling indices  $\mathcal{Z} = \{i_1, \dots, i_{n_f}\}$

$\Xi^\top \mathbf{Z} = \mathbf{QR}$ , where  $\mathbf{Q} \in \mathbb{R}^{r_f \times r_f}$ ,  $\mathbf{Q}^\top \mathbf{Q} = \mathbf{I}_{r_f}$ , and  $\mathbf{R} \in \mathbb{R}^{r_f \times N}$  is upper triangular.

Take  $\mathcal{Z} = \{i_1, \dots, i_{r_f}\}$ , with  $\mathbf{Z} = [\mathbf{e}_{i_1}, \dots, \mathbf{e}_{i_{r_f}}]$

**for**  $\ell = r_f + 1 : n_f$  **do**

Construct  $\mathbf{Z} = [\mathbf{e}_{i_1}, \dots, \mathbf{e}_{i_{\ell-1}}]$  from  $\mathcal{Z}$

$\mathbf{Z}^\top \Xi = \mathbf{USV}^\top$ , where  $\mathbf{U} \in \mathbb{R}^{j \times r_f}$ ,  $\mathbf{U}^\top \mathbf{U} = \mathbf{I}_j$ ,  $\mathbf{V} \in \mathbb{R}^{r_f \times r_f}$ ,  $\mathbf{V}^\top \mathbf{V} = \mathbf{I}_{r_f}$ , and

$\mathbf{S} \in \mathbb{R}^{r_f \times r_f}$  is diagonal

Compute  $g = \sigma_{r_f-1}^2 - \sigma_{r_f}^2$  where  $\mathbf{S} = \text{diag}(\sigma_1, \dots, \sigma_{r_f})$

Compute  $\mathbf{W} = \mathbf{V}^\top \Xi^\top \in \mathbb{R}^{r_f \times N}$

Compute  $\mathbf{y} = (\mathbf{W} \odot \mathbf{W})^\top \mathbf{1}_{r_f} \in \mathbb{R}^N$

$i_\ell = \text{argmax}_{i \notin \mathcal{Z}} (g + \mathbf{y}_i - \sqrt{(g + \mathbf{y}_i)^2 - 4g(\mathbf{W}_{r_f, i})^2})$

$\mathcal{Z} \leftarrow \mathcal{Z} \cup \{i_\ell\}$

**end for**

---

#### 4.1.1 DEIM

The discrete empirical interpolation method (DEIM) was introduced in [43] for greedily selecting  $n_f = r_f$  sampling indices from the linearly independent rows of  $\Xi$  such that the 2-norm of  $(\mathbf{Z}^\top \Xi)^+$  is minimized. A variant of this algorithm that allows for oversampling ( $n_f \geq r_f$ ) was introduced in [60], a simplified version of which is presented in Algorithm 1.

#### 4.1.2 Q-DEIM

The Q-DEIM algorithm was introduced in [45] as a variant of DEIM for selecting the sampling indices in a way that produces a smaller estimate of the condition number  $\|(\mathbf{Z}^\top \Xi)^+\|_2$  when  $n_f = r_f$ . In contrast to the greedy selection process employed in DEIM, the Q-DEIM algorithm relies on a rank revealing QR factorization of  $(\mathbf{Z}^\top \Xi)^\top$ . A further development of Q-DEIM termed GappyPOD+E was proposed in [61], which achieves low projection errors with few oversampling points by maximizing the lower bound of the smallest singular value of  $\mathbf{Z}^\top \Xi$ . This algorithm is presented in Algorithm 2.

#### 4.1.3 S-OPT

The majority of gappy POD-based methods for selecting  $\mathcal{Z}$  are based on the principle of minimizing the largest singular value of the sampled matrix  $(\mathbf{Z}^\top \Xi)^+$ . This is referred to as E-optimality [62] in the optimal design community and suffers from the issue of numerical instability [47]. On the other hand, the S-OPT algorithm introduced in [47]

---

**Algorithm 3** S-OPT sampling algorithm

---

**Input:** Basis matrix  $\Xi \in \mathbb{R}^{N \times r_f}$  and desired number of sampled indices  $n_f$ .

**Output:** A set of  $n_f$  indices  $\mathcal{Z} = \{i_1, \dots, i_{n_f}\}$ .

- 1:  $i_1 = \operatorname{argmax}_i |\Xi_{i,1}|$
  - 2:  $\mathcal{Z} = \{i_1\}$
  - 3: **for**  $\ell = 2 : r_f$  **do**
  - 4:   Construct  $\Xi^{(\ell-1)} = \Xi[e_1, \dots, e_{\ell-1}]$
  - 5:   Construct  $\mathbf{Z} = [e_{i_1}, \dots, e_{i_{\ell-1}}]$
  - 6:   Construct  $\mathbf{A} = \mathbf{Z}^\top \Xi^{(\ell-1)}$
  - 7:    $i_\ell = \operatorname{argmax}_{i \notin \mathcal{Z}} \frac{1 + \mathbf{r}^\top \mathbf{b}}{\prod_{k=1}^{\ell-1} (\|\mathbf{A} \mathbf{e}_k\|^2 + \mathbf{r}_k^2)} \frac{\mathbf{c}^\top \mathbf{c} + \gamma^2 - \alpha}{\mathbf{c}^\top \mathbf{c} + \gamma^2}$ , with  
$$\mathbf{r}^\top = \mathbf{e}_i^\top \Xi^{(\ell-1)}, \quad \mathbf{b} = (\mathbf{A}^\top \mathbf{A})^{-1} \mathbf{r}, \quad \gamma = \Xi_{i,\ell}$$
  - 8:    $\mathcal{Z} \leftarrow \mathcal{Z} \cup \{i_\ell\}$
  - 9: **end for**
  - 10: **for**  $\ell = r_f + 1 : n_f$  **do**
  - 11:   Construct  $\mathbf{Z} = [e_{i_1}, \dots, e_{i_{\ell-1}}]$
  - 12:   Construct  $\mathbf{A} = \mathbf{Z}^\top \Xi$
  - 13:    $i_\ell = \operatorname{argmax}_{i \notin \mathcal{Z}} \frac{1 + \mathbf{r}^\top (\mathbf{A}^\top \mathbf{A})^{-1} \mathbf{r}}{\prod_{k=1}^{\ell-1} (\|\mathbf{A} \mathbf{e}_k\|^2 + \mathbf{r}_k^2)}$ , with  $\mathbf{r}^\top = \mathbf{e}_i^\top \Xi$
  - 14:    $\mathcal{Z} \leftarrow \mathcal{Z} \cup \{i_\ell\}$
  - 15: **end for**
- 

pursues S-optimality, which results in better numerical stability than sampling methods based on E-optimality. The core principle of S-OPT is to simultaneously promote the nonsingularity of the normal matrix  $(\mathbf{Z}^\top \Xi)^\top \mathbf{Z}^\top \Xi$  and the column orthogonality of the sampled matrix  $\mathbf{Z}^\top \Xi$  by maximizing measure  $\mathcal{S}$  [63]

$$\mathcal{S}(\mathbf{Z}^\top \Xi) = \left( \frac{\sqrt{\det \left( (\mathbf{Z}^\top \Xi)^\top \mathbf{Z}^\top \Xi \right)}}{\prod_{k=1}^p \|\mathbf{Z}^\top \Xi \mathbf{e}_k\|_2} \right)^{\frac{1}{p}}. \quad (18)$$

The S-OPT algorithm as described in [47, Algorithm 1] is presented in Algorithm 3. In the developed algorithm, the determinant computations are performed using a fast method that exploits the rank-one updates involved in each iteration [63, Section 3.3.3].

## 4.2 Quadrature methods

An alternative to interpolation hyper-reduction methods is the empirical quadrature procedure (EQP) [52], which approximates the evaluation of  $\mathbf{f}$  by a sparse approximate quadrature rule. Recalling (4), each entry  $\mathbf{f}_j$  is computed from an integral involving the test function  $\varphi_j$  and the action of  $f$  on the associated trial function  $y_h = L_{\mathcal{B}_y}^{-1}(\mathbf{y})$  on a domain  $\tilde{\Omega}$

$$\mathbf{f}_j(\mathbf{y}, t) = \langle f(y_h, t), \varphi_j \rangle_{\mathcal{V}' \times \mathcal{V}} = \int_{\tilde{\Omega}} \eta(y_h, \varphi_j, t, x) dx \quad (19)$$

with  $\eta : \mathcal{Y}^h \times \mathcal{Y}^h \times [0, T] \times \tilde{\Omega} \rightarrow \mathbb{R}$  denoting the integrand. In the numerical implementation of finite element methods, such integrals are approximated using numerical quadrature rules as a weighted sum of integrand evaluations at a collection of  $K \in \mathbb{N}$  sample points  $\{x_k\}_{k=1}^K \subset \tilde{\Omega}$  with corresponding positive weights  $\{\rho_k\}_{k=1}^K$

$$\mathbf{f}_j(\mathbf{y}, t) \approx \sum_{k=1}^K \rho_k \eta(y_h, \varphi_j, t, x_k). \quad (20)$$

EQP seeks to form a sparse approximation of the weighted sum (20), where the new weights  $\rho_k^*$  are all zero except at a few sampled quadrature points

$$\mathbf{f}_j(\mathbf{y}, t) \approx \sum_{k=1}^K \rho_k^* \eta(y_h, \varphi_j, t, x_k) \quad (21)$$

with  $|\{k: \rho_k^* \neq 0\}| = K^* \ll K$ . The computational expense of calculating  $\mathbf{f}$  scales with the number of sampled quadrature points, making it desirable to minimize  $K^*$ . At the same time, the set of nonzero quadrature weights affects the quality of the approximation in (21), which in turn has a significant impact on the downstream ROM accuracy (in analogy to the role of  $\mathcal{Z}$  in interpolation methods). It is therefore desirable to obtain a vector of weights  $\boldsymbol{\rho}^*$  that minimizes  $K^*$  while keeping the approximation error below a chosen tolerance.

The task of computing  $\boldsymbol{\rho}^*$  has been formulated as a linear programming problem [52] and as an equivalent nonnegative least squares (NNLS) problem [64, 65]. In this work we follow the latter approach and determine  $\boldsymbol{\rho}^*$  by solving the NNLS problem

$$\boldsymbol{\rho}^* = \arg \min_{\mathbf{r} \geq 0} \|\mathbf{G}\boldsymbol{\rho} - \mathbf{G}\mathbf{r}\|_2^2 \quad (22)$$

where  $\mathbf{G} \in \mathbb{R}^{n_c \times K}$  is an accuracy constraints matrix with  $n_c$  constraint rows and  $\boldsymbol{\rho}$  is the original quadrature weights vector. The entries of each row of  $\mathbf{G}$  correspond to the evaluation of the integrand at all FOM quadrature points  $x_k$  for a given combination of FOM trial functions  $y_h$ , test functions  $\varphi_j$  and time points  $t_s$ . More specifically, we define the entries of  $\mathbf{G}$  as

$$\mathbf{G}_{ik} = \eta(y_h(t_s)\varphi_j, t_s, x_k) \quad 1 \leq s \leq n_t \quad 1 \leq j \leq r_y \quad (23)$$

with overall constraint index  $1 \leq i = j + (s - 1)r_y \leq n_c$  and  $y_h(t_s)$  the snapshot of the FOM state at time  $t_s$ . We set the number of constraints to  $n_c = n_t r_y \ll K$ , which corresponds to  $r_y$  constraints (one for each component of  $\mathbf{f}$ ) for every snapshot time  $t_s$ . The above formulation of the NNLS constraints can be readily generalized to parametric problem cases, where multiple solution snapshots (one for each parameter value considered) are collected at every time value  $t_s$ . Even though the NNLS problem (22) does not attempt to explicitly minimize  $K^*$ , we find that significantly sparse solutions  $\boldsymbol{\rho}^*$  are obtained in our numerical experiments, matching the behavior demonstrated in previous works [64, 65].

After forming  $\mathbf{G}$ , the NNLS problem (22) is solved using the Lawson-Hanson algorithm [66]. Before applying the algorithm, two conditioning operations are performed on  $\mathbf{G}$ , which we have found to increase the derived quadrature rule's accuracy and decrease the number of iterations needed for the algorithm's convergence. First, each row of  $\mathbf{G}$  is rescaled by dividing the row by its maximum absolute value. In our numerical experiments we have found that within each row, nonzero entries may differ considerably in magnitude. Rescaling all entries to take values within  $[-1, 1] \subset \mathbb{R}$  was found to improve the convergence of the Lawson-Hanson algorithm. Second, we compute the LQ decomposition of matrix  $\mathbf{G} = \mathbf{L}\mathbf{Q}$  and use matrix  $\mathbf{Q}$  as the constraints matrix. It has been previously reported that using a constraints matrix with orthonormal rows (constraints) consistently reduces the number of iterations needed for the Lawson-Hanson algorithm to converge [67], and this indeed matches our own experience. Additional details on the implementation of the EQP method and the NNLS formulation can be found in [28]. Finally, we note that generally the resulting sparse quadrature rule can only be expected to yield accurate solutions in the neighborhood of the state snapshots  $y_h(t_s)$  used for forming  $\mathbf{G}$ . If desired, additional snapshots can be incorporated into  $\mathbf{G}$  to make the derived quadrature rule more robust. However, increasing the number of snapshots will increase the offline time spent solving the NNLS problem and may also increase the resulting number of nonzero entries of  $\boldsymbol{\rho}^*$ .

## 5 Numerical results

The inherent tradeoff for any hyper-reduction method between minimizing computational time and maximizing approximation accuracy can be quantified with a Pareto front.

**Definition 5.1** (Pareto front) *Given a finite solution set  $\mathcal{D} = \{\mathbf{x}_1, \mathbf{x}_2, \dots, \mathbf{x}_n\}$  and  $m$  objective functions  $f_1, f_2, \dots, f_m$ , the Pareto front  $\mathcal{P}$  is defined as the set of solutions  $\mathbf{x}^* \in \mathcal{D}$  for which no  $\mathbf{x} \in \mathcal{D}$  satisfies both*

$$f_i(\mathbf{x}) \leq f_i(\mathbf{x}^*) \text{ for all } i \in \{1, \dots, m\} \text{ and } f_j(\mathbf{x}) < f_j(\mathbf{x}^*) \text{ for some } j \in \{1, \dots, m\}.$$

In this study, we consider the case  $m = 2$ , with relative online phase computation time and relative  $L^2$  error between FOM and ROM solutions as the two Pareto front objective functions. It is expected that the Pareto front, and thus the optimal choice of hyper-reduction method, will vary for different problems.

**Table 1:** Summary of simulation setups.

Problem	ODE solver	$T$	FE DOFs	FE order		$N_t$
				Kin.	Th.	
Nonlinear diffusion	Backward Euler	0.1	3136	0	–	100
Nonlinear elasticity	RK4	5.0	2340	2	–	500
Sedov blast	RK4	0.2	33574	2	1	363
	RK2Avg					377
Taylor-Green	RK4	0.1	33574	2	1	266
	RK2Avg					266
Triple point	RK4	0.5	87702	2	1	95
	RK2Avg					95

The hyper-reduction methods introduced in Section 4 are applied to five problems: nonlinear diffusion (Section 5.1), nonlinear elasticity (Section 5.2) and three Lagrangian hydrodynamics problems: Sedov blast (Section 5.3.1), Taylor-Green vortex (Section 5.3.2) and triple point (Section 5.3.3). Detailed settings for these problems are summarized in Table 1, including the ODE solver, final time ( $T$ ), number of finite element degrees of freedom, finite element polynomial order, and the number of time steps ( $N_t$ ) for FOM runs. For each considered problem case, the physical quantities are parametrized with  $\boldsymbol{\mu} \in \mathcal{D}$ . Figure 1 visualizes the final-time FOM solutions in various benchmark problems.

The computations conducted for each problem are split into two stages: the offline and online stages. In the offline (training) stage we use the available full order model to build (train) the reduced order model that will be used in the following online stage. To that end, we perform FOM simulations and collect  $s \in \mathbb{N}$  snapshots of the state variables  $\boldsymbol{x}(t) \in \mathbb{R}^{N_y}$  corresponding to various time values  $t$  and physical parameters  $\boldsymbol{\mu} \in \mathcal{D}$ . The snapshots are used to form the snapshot matrix  $\boldsymbol{X} \in \mathbb{R}^{N_y \times s} = [\boldsymbol{x}(0), \dots, \boldsymbol{x}(T)]$ , which is then used to derive the ROM basis. More specifically, we compute the singular value decomposition (SVD)  $\boldsymbol{X} = \boldsymbol{U}\boldsymbol{\Sigma}\boldsymbol{V}^\top$  of  $\boldsymbol{X}$  and use the first  $r_y$  columns of  $\boldsymbol{U} \in \mathbb{R}^{N_y \times s}$  (left singular vectors) to form the ROM basis matrix  $\boldsymbol{\Psi} \in \mathbb{R}^{N_y \times r_y}$ . The left singular vectors of  $\boldsymbol{X}$  correspond to the eigenvectors of the symmetric matrix  $\boldsymbol{X}\boldsymbol{X}^\top \in \mathbb{R}^{N_y \times N_y}$ , which is the temporal correlation kernel matrix usually employed in POD [68–70].

To choose the number of ROM basis vectors  $r_y$  we use the “energy” content of the snapshot matrix  $\boldsymbol{X}$  and associated ROM basis matrix  $\boldsymbol{\Psi}$ , which is given by the sum of their respective squared singular values

$$E_{tot} = \sum_{i=1}^r \sigma_i^2 \quad E_c = \sum_{i=1}^{r_y} \sigma_i^2$$

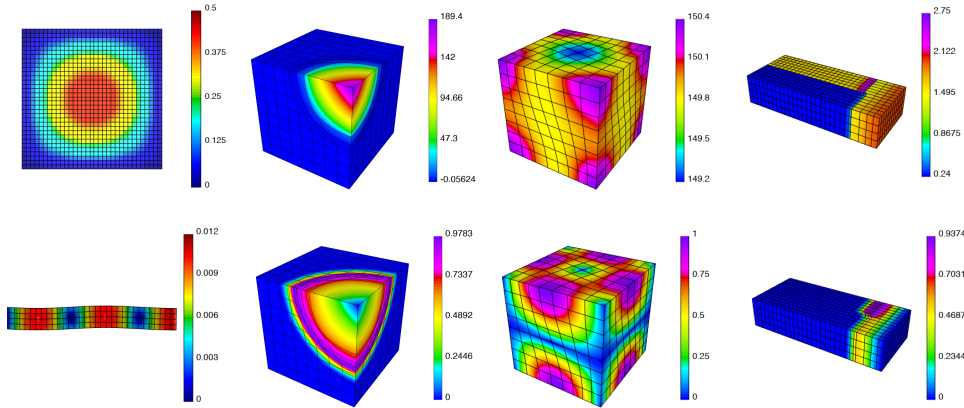


**Fig. 1:** Visualization of final-time fields from FOM simulations. The first column shows the nonlinear diffusion problem (top, temperature) and the nonlinear elasticity problem (bottom, velocity). The remaining columns correspond to Lagrangian benchmark problems, showing energy (top) and velocity (bottom) for the Sedov blast (second column), the Taylor-Green vortex (third column), and the triple-point problem (fourth column).

where  $r = \text{rank}(\mathbf{X})$  and  $r_y \leq r$ . For a given choice of snapshot and ROM basis matrices, the residual energy fraction is then given by

$$E_r = -\log_{10}(1 - (E_c/E_{tot})) \quad (24)$$

where the required number of ROM basis vectors increases with increasing residual energy fraction. In the numerical experiments that follow we focus on residual energy fraction values  $E_r \in \{1, 2, 3, 4, 5, 6\}$ .

After forming the ROM basis matrix  $\Psi$ , the remainder of the offline stage is devoted to computing the quantities needed by the chosen hyper-reduction method. For interpolation methods, this involves forming the nonlinear force basis matrix  $\Xi$  and sampling matrix  $\mathbf{Z}$  introduced in Section 4.1. The basis matrix  $\Xi$  is formed by the same procedure outlined above for  $\Psi$ , using snapshots for the nonlinear force vector  $\mathbf{f}$  instead of the state variables. When applicable, the same approach is employed to construct a basis for  $\mathbf{g}$ . The construction of the sampling matrix  $\mathbf{Z}$  follows the algorithms presented in Sections 4.1.1–4.1.3 depending on the chosen sampling method (DEIM, Q-DEIM or S-OPT). For the EQP method, the offline stage involves computing the vector of sampled quadrature weights  $\rho^*$  introduced in Section 4.2. This requires solving the NNLS problem (22) with the appropriate constraints matrix  $\mathbf{G}$ , and is done once for each nonlinear force vector  $\mathbf{f}$  and  $\mathbf{g}$ . Regardless of the specific hyper-reduction method used, for simulations consisting of multiple time windows (Section 5.3), the computation of the basis matrix  $\Psi$  and the hyper-reduction related quantities is performed once for each time window.

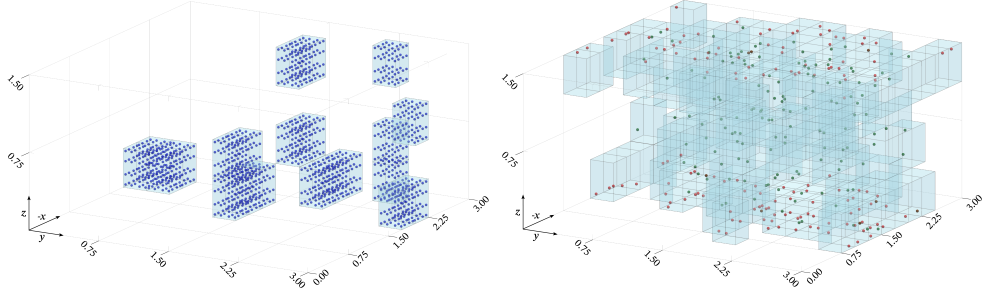


**Fig. 2:** Sample mesh comparison for the triple point problem. Left: S-OPT sample mesh with 22 sampled elements and  $22 \times 64 = 1408$  sampled quadrature points (in dark blue). Right: EQP sample mesh with 178 sampled elements and 150 sampled quadrature points each for the energy field (in green) and the velocity field (in red).

The second stage of computations is the online stage, where we use the reduced model built in the offline stage to simulate the considered dynamics. The online simulations can be of one of two categories: reproductive or predictive. In reproductive simulations we use the formed reduced model to simulate the system for initial conditions and/or parameter values that were used in its training (offline stage). Reproductive runs are used to quantify the reduced model’s performance in reproducing its training data. On the other hand, in predictive simulations we evaluate the reduced model using initial conditions and/or parameter values that were not used in its training. As a result, predictive runs are used to test the ability of a given reduced model to generalize beyond its training data.

The hyper-reduction methods tested in this work require the selection of the number of sampling points ( $n_f$  for gappy POD methods and  $K^*$  for EQP). Ideally, this selection is done such that the nonlinear functions  $\mathbf{f}$  and  $\mathbf{g}$  are accurately approximated while the computation time is minimized. However, the relation between the number of sampling points and the resulting computation time is not always straightforward.

Our implementation of the tested hyper-reduction methods relies on the construction of a *sample mesh*, which consists of the finite elements containing the sampled quadrature or interpolation points. Each finite element in our computational domain includes a prescribed number of FEM basis functions (degrees of freedom) and associated quadrature points. The interpolation hyper-reduction methods sample degrees of freedom, corresponding to the  $n_f$  sampled indices  $\mathcal{Z}$ . Their implementation requires the evaluation of the sampled degrees of freedom at all local quadrature points. On the contrary, the EQP method samples quadrature points, determined by the  $K^*$  non-zeros resulting from solving the NNLS problem (22). Its implementation requires the evaluation of all local degrees of freedom at the subset of sampled quadrature points. Because of this difference in approach between the two classes of methods, the computational cost of the tested hyper-reduction methods depends on element-wise factors that go beyond the number of sampled points.

In many cases, the EQP method can also be implemented using pointwise integration, effectively viewing the whole computational domain as one “global element” to bypass the need for a sample mesh [64]. This is possible when the nonlinear terms allow for a clean offline-online splitting, where the geometric mapping and basis function gradients are precomputed in a fixed reference configuration.

However, for the Lagrangian hydrodynamics problems (Section 5.3), the computational mesh is continuously deforming with time, while the governing equations involve complex state-dependent terms such as artificial viscosity that rely on local spatial stencils. Specifically, robust shock-capturing via artificial viscosity necessitates the calculation of velocity gradients and characteristic length scales derived from the instantaneous configuration of the local mesh [58]. Evaluating these element-based terms requires the online reconstruction of local geometric quantities (e.g., Jacobians and velocity gradients) and neighborhood connectivity at each time step. Since these geometric quantities evolve dynamically and are inextricably linked to the mesh topology, they cannot be fully precomputed in a fixed reference configuration. While alternative FOM discretizations (e.g., purely pointwise artificial viscosity) might allow for a fully mesh-independent implementation, they often lack the robustness required for complex shock-physics. As a result, the standard formulations used in the present work require access to the local mesh structure.

This complex relationship between the sample mesh and ROM cost can lead to situations where using fewer sampled points does not necessarily lead to lower computational cost. Anticipating our later discussion, Figure 2 illustrates such a scenario for the triple point problem (Section 5.3.3), where the sampled elements are visualized as volumes and the sampled points as dots. In this particular example, although fewer points are sampled by EQP than by S-OPT, the points sampled by EQP are scattered across many high order elements. This means that the sample mesh obtained by EQP contains significantly more elements than the one obtained by S-OPT. In such a case, the computational overhead associated with loading the sampled elements and reconstructing their local geometry can outweigh the savings gained from reducing the total number of quadrature points. As a result, the hyper-reduction speed-up becomes heavily dependent on the spatial distribution of the sampled points and the spatial sparsity of the sampled elements, rather than just the number of sampled quadrature points. These observations help highlight a key message: the employed FOM discretization can be an important factor in determining the speedup that can be delivered by a chosen hyper-reduction method.

As explained earlier, in the results that follow we use the  $L^2$  error between FOM and ROM solutions to quantify the error introduced by the different hyper-reduction methods for each problem case. In addition to the hyper-reduction error, there are two additional sources of error included in the reported  $L^2$  error values: (1) the projection error introduced by restricting the dynamics to a linear subspace of the original state space; (2) for predictive simulation runs, the sampling error introduced when sampling each problem’s parameter space. The reason the  $L^2$  FOM-to-ROM error can be employed to perform a fair comparison between different hyper-reduction methods is that the projection and sampling errors are constant among the different hyper-reduction methods for each problem case. This is because: (1) the same

linear subspaces are used across all simulations within each problem case; (2) the same parameter values are sampled for training and used for out-of-sample testing for each problem. As such, even though the magnitude of the reported FOM-to-ROM errors includes additional error sources, their relative *difference* depends only on the employed hyper-reduction methods, allowing for fair comparisons within each problem case.

## 5.1 Nonlinear diffusion

We consider the nonlinear diffusion equation in  $\Omega \subset \mathbb{R}^2$

$$\begin{aligned} \frac{\partial p}{\partial t} - \nabla \cdot v &= s(t) & \text{in } \Omega \times (0, T) \\ \nabla p - \kappa(p)^{-1}v &= 0 & \text{in } \Omega \times [0, T] \\ v \cdot n &= 0 & \text{on } \partial\Omega \times [0, T] \\ p &= p_0 & \text{in } \Omega \times \{0\} \end{aligned} \quad (25)$$

where  $p \in L^2(\Omega)$  denotes the pressure,  $v \in H_0(\text{div}; \Omega) = \{\psi \in \mathcal{H}(\text{div}; \Omega) : \psi \cdot n = 0\}$  the flux and  $s: (0, T) \rightarrow L^2(\Omega)$  a time dependent external source function.

To fit the nonlinear diffusion equation (25) into the general variational framework (2) introduced in Section 2 we identify the following components. The dependent variables are given by  $y = p$  and  $z = v$ , with associated vector spaces  $\mathcal{Y} = L^2(\Omega)$ ,  $\mathcal{Z} = H_0(\text{div}; \Omega)$  and  $\mathcal{H} = L^2(\Omega)$  with the standard  $L^2$  inner product  $(\cdot, \cdot)_{\mathcal{H}}$ , leading to the trivial Gelfand triple  $\mathcal{Y} = \mathcal{H} = \mathcal{Y}'$ . The bilinear forms  $a: \mathcal{Y} \times \mathcal{Y} \rightarrow \mathbb{R}$ ,  $b: \mathcal{Y} \times \mathcal{Z} \rightarrow \mathbb{R}$  and  $c: \mathcal{Z} \times \mathcal{Z} \rightarrow \mathbb{R}$  are defined as

$$a(p, p') = 0 \quad b(p, v) = - \int_{\Omega} p(\nabla \cdot v) dx \quad c(v, v') = 0$$

for any  $p, p' \in \mathcal{Y}$  and  $v, v' \in \mathcal{Z}$ . Finally, the duality pairing involving the nonlinear functions  $f: \mathcal{Y} \times \mathcal{Z} \times (0, T) \rightarrow \mathcal{Y}'$  and  $g: \mathcal{Y} \times \mathcal{Z} \times (0, T) \rightarrow \mathcal{Z}'$  are given by

$$\langle f(p, v, t), p' \rangle_{\mathcal{Y}' \times \mathcal{Y}} = \int_{\Omega} s(t)p' dx \quad \langle g(p, v, t), v' \rangle_{\mathcal{Z}' \times \mathcal{Z}} = \int_{\Omega} -\kappa(p)^{-1}v \cdot v' dx$$

for any  $(p, v, t) \in \mathcal{Y} \times \mathcal{Z} \times (0, T)$ ,  $p' \in \mathcal{Y}$  and  $v' \in \mathcal{Z}$ .

To generate our numerical results we consider a two dimensional problem defined on the unit square  $\Omega = [0, 1]^2$ . The initial condition for pressure is given by

$$p_0(x, y) = \begin{cases} 1 & \text{if } \max_{i=1,2} |x_i - 0.5| < \mu \\ 0 & \text{otherwise} \end{cases}$$

where parameter  $\mu \in [0, 0.5]$  and  $(x, y) \in \Omega$ , with conductivity  $\kappa(p) = 2.0 + p$  and source  $s = 0$ . We perform the spatial discretization using a mixed finite element formulation, with the finite element spaces chosen such as to satisfy the inf-sup condition for

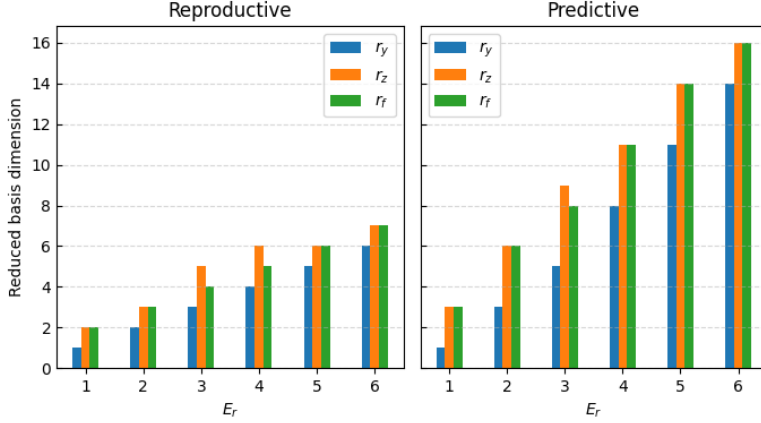


**Fig. 3:** Reduced basis dimensions with respect to the residual energy fraction for the nonlinear diffusion simulations.

stable mixed formulations. In particular, the pressure  $p$  is approximated in  $\mathcal{V}_P^h \subset L^2(\Omega)$  and the flux  $v$  in  $\mathcal{V}_V^h \subset H_0(\text{div}; \Omega)$ . The FE coefficient vector functions for pressure and flux are denoted respectively by  $\mathbf{p}(t) \in \mathbb{R}^{N_P}$  and  $\mathbf{v}(t) \in \mathbb{R}^{N_V}$ , with  $N_P$  and  $N_V$  the corresponding total numbers of degrees of freedom. The semi-discretized form of the governing equation (25) is then expressed as a system of differential-algebraic equations with  $N_y = N_P$  and  $N_z = N_V$ .

We perform both reproductive and predictive simulation runs, with a range of residual energy fractions summarized in Figure 3. For the reproductive case we consider the parameter value  $\mu = 0.3$  and keep it fixed for both the offline and online stages. The predictive case tests the ROM's capacity for predicting simulation data not seen during its training, which means that we use different values of  $\mu$  for the offline and online stages. More specifically, in what follows we present results generated by using  $\mu \in \{0.15, 0.25, 0.35\}$  for training and  $\mu = 0.3$  for prediction.

Figure 4 compares the performance of reduced simulations with different hyper-reduction methods across a range of residual energy fractions. In every figure panel, the Pareto front between  $L^2$  error of the pressure field, on the vertical axis, and number of sampled points on the horizontal axis, is shown for the different hyper-reduction methods. We note that the Pareto front points are optimal with respect to computational time and error, not necessarily with respect to the number of sampled interpolation/quadrature points. Every figure panel also includes a solid black line at relative error  $10^{-2}$  that serves as a reference baseline for comparisons across all methods.

A convergence to low relative error levels is observed for both interpolation methods and EQP as the residual energy fraction (or equivalently, ROM basis dimensions) increases. At  $E_r = 6$  all methods in the reproductive case reach a relative error of about  $10^{-3}$ , whereas for the predictive case the lowest relative error is approximately  $10^{-4}$ . In both reproductive and predictive runs the error levels of the interpolation

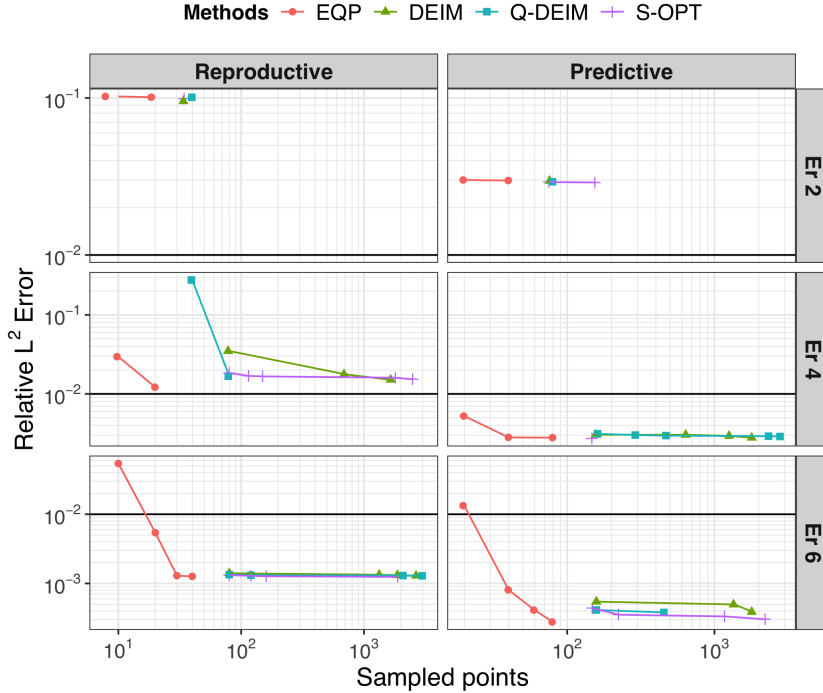


**Fig. 4:** Performance comparison for the nonlinear diffusion ROM simulations with varying number of sampled interpolation/quadrature points. The left column shows reproductive simulation results, while the right one predictive results. The top row corresponds to residual energy fraction  $E_r = 2$ , the middle row to  $E_r = 4$  and the bottom one to  $E_r = 6$ .

methods seems to correlate with  $E_r$  and not with the number of sampled interpolation points. On the contrary, the EQP error levels demonstrate a tendency to decrease as the number of quadrature points increases, especially when  $E_r$  is large. The lowest error levels obtained by each method are approximately of the same order of magnitude for this problem case. However, the EQP method seems to generally require a smaller number of quadrature points to reach a given error level.

The tradeoff between computational cost and relative error is made explicit in Figure 5, which depicts the Pareto fronts obtained for each hyper-reduction method among all values of  $E_r$ . The overall Pareto front is drawn as a line connecting the most efficient configurations across all methods. In the reproductive case the overall Pareto front consists entirely of EQP method simulations. The lowest error level achieved is about  $10^{-3}$ , at which point EQP records a relative online time of approximately  $4 \times 10^{-3}$ , while the interpolation methods record about  $6 \times 10^{-3}$ . In the predictive scenario, although EQP shows greater efficiency for higher error levels, a tradeoff appears as the error levels decrease. More specifically, at error levels below  $10^{-3}$  or

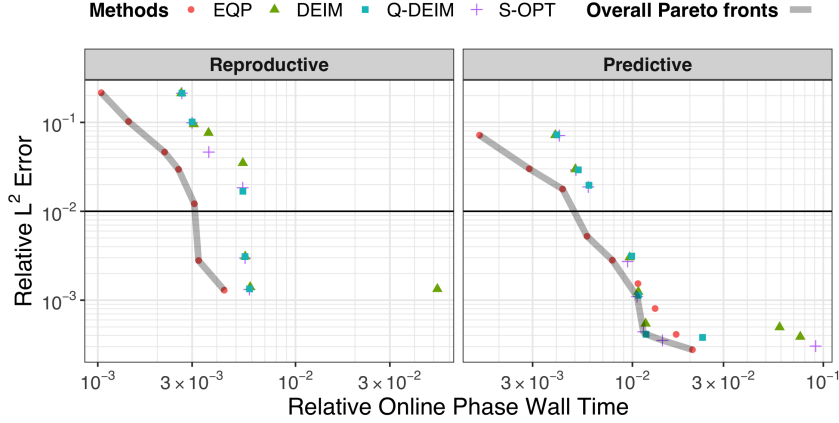


**Fig. 5:** Overall Pareto fronts across all hyper-reduction methods for the nonlinear diffusion problem, illustrating the tradeoff between relative  $L^2$  error and online phase wall time.

when the relative online time exceeds  $10^{-2}$ , the interpolation methods emerge on the overall Pareto front.

To summarize, for the nonlinear diffusion problem, the Pareto optimal method is EQP in the reproductive case as well as in the predictive case for error levels above  $10^{-3}$ . For lower predictive error levels, interpolation methods also appear on the Pareto front, with no method consistently outperforming the others. The observed lower error levels in the predictive scenario compared to the reproductive one could be explained by the larger number of basis vectors retained for the same energy residual as shown in Figure 3. Furthermore, the samples taken in the offline stage seem to describe the system conditions tested in the online stage well. If one were to sample  $\mu$  further away from its online stage value, then the obtained error would be expected to rise.

## 5.2 Nonlinear elasticity

We consider the dynamics of a visco-hyperelastic solid of homogeneous neo-hookean material. The state of the medium is described as a function of time  $t$  and reference coordinates of the material particles  $\tilde{x} \in \tilde{\Omega} = \Omega(0)$  at initial time  $t = 0$ . The system evolves over the reference configuration  $\tilde{\Omega}$  according to the equations

$$\begin{aligned}
 \rho \frac{dv}{dt} &= H(x) + \eta \Delta v && \text{in } \tilde{\Omega} \times (0, T) \\
 \frac{dx}{dt} &= v && \text{in } \tilde{\Omega} \times (0, T) \\
 v &= 0 && \text{on } \Gamma_{\text{in}} \times (0, T) \\
 n \cdot \nabla v &= 0 && \text{on } (\partial \tilde{\Omega} \setminus \Gamma_{\text{in}}) \times (0, T)
 \end{aligned} \tag{26}$$

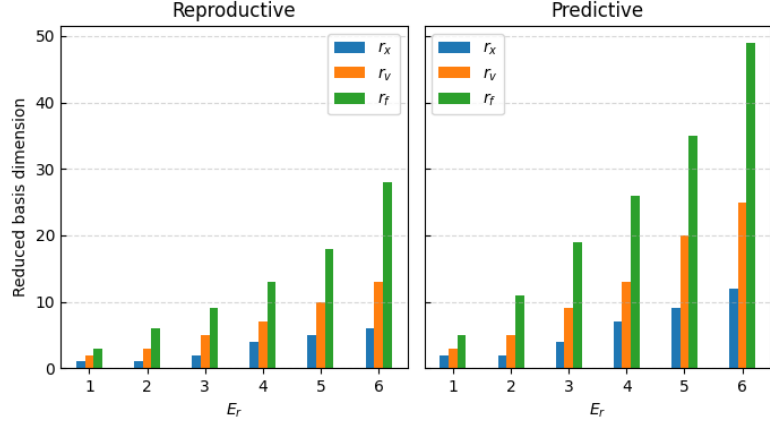


**Fig. 6:** Reduced basis dimensions used for each residual energy fraction in the non-linear elasticity simulations.

where  $x$  and  $v$  denote the solid's deformation and velocity fields, while  $\rho$  and  $\eta$  are the constant reference density and viscosity of the material in its initial configuration. In addition,  $d/dt$  denotes the material derivative and  $n$  the normal vector on the boundary  $\partial\tilde{\Omega}$ ; the spatial differential operators act with respect to the reference coordinates  $\tilde{x}$ . The nonlinear function  $H: H_{0,\Gamma_{\text{in}}}^1(\tilde{\Omega}) \rightarrow H_{\Gamma_{\text{in}}}^{-1}(\tilde{\Omega})$ ,  $H(x) = \nabla \cdot \mathbf{P}(x)$  is the divergence of the first Piola-Kirchhoff stress tensor.

To write the nonlinear elasticity equations (26) in the general variational form (2) we make the following identifications. We use the state variable  $y = (v, x)$  with state space  $\mathcal{Y} = [H^1(\tilde{\Omega})]^d \times [H^1(\tilde{\Omega})]^d$  and Hilbert space  $\mathcal{H} = [L^2(\tilde{\Omega})]^d \times [L^2(\tilde{\Omega})]^d$ . There is no algebraic variable  $z$  in this problem case. The inner product  $(\cdot, \cdot)_{\mathcal{H}}: \mathcal{H} \times \mathcal{H} \rightarrow \mathbb{R}$  and bilinear form  $a: \mathcal{Y} \times \mathcal{Y} \rightarrow \mathbb{R}$  are given by

$$((v, x), (v', x'))_{\mathcal{H}} = \int_{\tilde{\Omega}} \rho v \cdot v' + x \cdot x' d\tilde{x} \quad a((v, x), (v', x')) = \int_{\tilde{\Omega}} \eta \nabla v : \nabla v' - v \cdot x' d\tilde{x}.$$

Finally, the nonlinear function  $f: \mathcal{Y} \times (0, T) \rightarrow \mathcal{Y}'$  is defined by its action

$$\langle f(v, x, t), (v', x') \rangle_{\mathcal{Y}' \times \mathcal{Y}} = \int_{\tilde{\Omega}} -\mathbf{P}(x) : \nabla v' d\tilde{x}$$

where  $\mathcal{Y}'$  denotes the dual of  $\mathcal{Y}$  with respect to  $(\cdot, \cdot)_{\mathcal{H}}$ .

Our numerical results are generated for a two dimensional problem defined on the rectangular domain  $\tilde{\Omega} = [0, 8] \times [0, 1]$ . The velocity initial condition is parametrized by  $\mu \in \mathbb{R}$  and given by

$$v_1(x, 0) = 0 \quad v_2(x, 0) = -\frac{\mu}{80} \sin(\mu x_1)$$

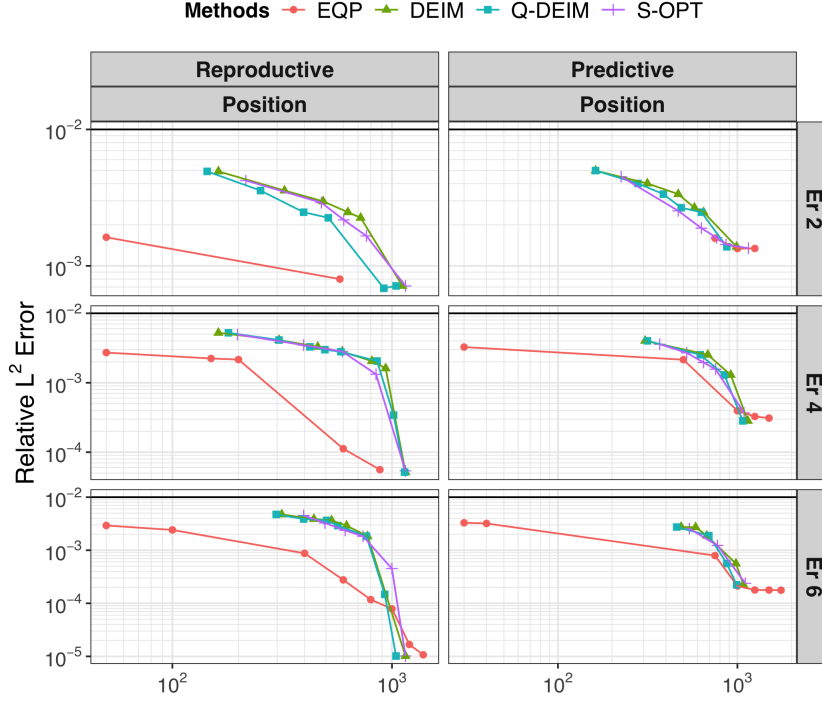


**Fig. 7:** Comparison of the ROM position errors for the nonlinear elasticity problem with varying number of sampled interpolation/quadrature points.

with  $x = (x_1, x_2) \in \tilde{\Omega}$ . The stress tensor  $\mathbf{P}$  is derived from a strain energy density function  $\Psi$  that involves the shear modulus  $\nu$  and bulk modulus  $K$  of the material and depends nonlinearly on the deformation gradient  $\mathbf{J}$  and its determinant  $J = |\mathbf{J}|$

$$\Psi(\mathbf{J}) = \frac{\nu}{2}(\bar{I}_1 - 2) + \frac{K}{2}(J/g - 1)^2$$

where  $g$  is a reference volumetric scaling and  $\bar{I}_1 = \text{tr}(\mathbf{J}^\top \mathbf{J})/J$ , yielding the stress tensor

$$\mathbf{P} = \frac{\nu}{J} \cdot \mathbf{J} + \left( \frac{KJ(J-g)}{g^2} - \frac{\nu \text{tr}(\mathbf{J}^\top \mathbf{J})}{2J} \right) \mathbf{J}^{-\top}.$$

For the spatial discretization of the nonlinear elasticity equations we use a single finite element space  $\mathcal{V}_V^h \subset [H^1(\tilde{\Omega})]^d$  to approximate the position and velocity fields. The FE coefficient vector functions for velocity and position are respectively denoted by  $\mathbf{v}(t) \in \mathbb{R}^{N_V}$  and  $\mathbf{x}(t) \in \mathbb{R}^{N_V}$ , each with a total of  $N_V$  degrees of freedom in  $\mathcal{V}_V^h$ . The semi-discretized form of (26) is then written as a system of ordinary differential equations with  $N_y = 2N_V$ . We partition the state variable  $y$  into the velocity  $v$  and

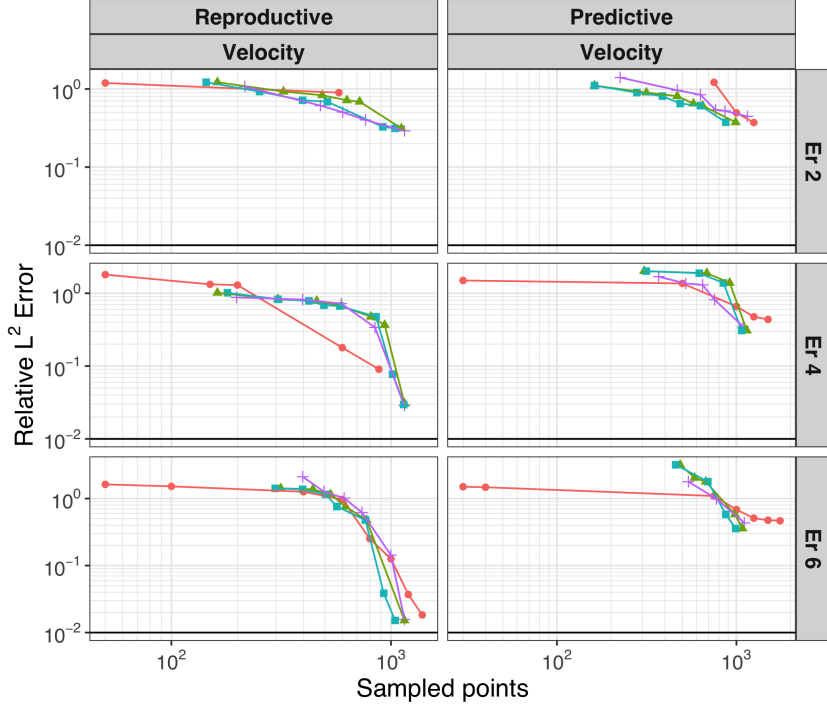


**Fig. 8:** Comparison of the ROM velocity errors for the nonlinear elasticity problem with varying number of sampled interpolation/quadrature points.

position  $x$  variables of equal full dimension. Each of the two variables is reduced independently during the formation of our reduced model, with their respective reduced dimensions denoted by  $r_v$  and  $r_x$ . The overall reduced state dimension  $r_y = r_x + r_v$  is then given by the sum of the two reduced dimensions.

To test the performance of different hyper-reduction methods we perform both reproductive and predictive simulations. For the reproductive case we use the parameter value  $\mu = 1.0$  for both the offline and online stages. For the predictive simulations we set  $\mu \in \{0.9, 1.1\}$  for the offline stage and  $\mu = 1.0$  for the online. The reduced basis dimensions obtained for each tested residual energy fraction are shown in Figure 6.

Figures 7 and 8 present an analogous comparison to that in Figure 4, with the position and velocity error results shown separately. The plotted points represent Pareto-optimal configurations for each hyper-reduction method, where the solution error is summarized by the  $L^2$ -product norm of the error in the state  $(v, x)$ . The results demonstrate that for all methods the relative errors decrease as the number of interpolation/quadrature points increases. We note that the error levels for position are noticeably smaller than those for velocity. For position errors, in both the reproductive and predictive scenarios, EQP generally attains a given error level with fewer quadrature points than the interpolation methods. At the lowest error levels, however,

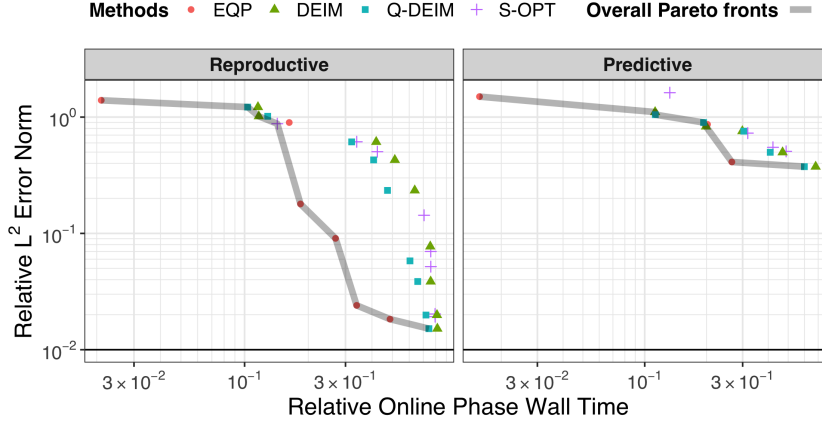


**Fig. 9:** Overall Pareto fronts across all hyper-reduction methods for velocity in the nonlinear elasticity problem.

the efficiency gain becomes marginal or, in some cases, EQP requires more quadrature points to reach comparable accuracy. The performance among the interpolation methods are relatively similar. For the velocity field, in the reproductive scenarios, the interpolation methods achieves significant lower velocity error levels than EQP when using a small residual energy fraction, whereas at larger energy residuals all methods perform comparably well. In the predictive scenario, except for cases with large energy residuals and few quadrature points, interpolation methods show better efficiency than EQP in terms of the quadrature points. Overall, EQP tends to exhibit better efficiency at higher error levels, while interpolation-based methods are more efficient at lower error levels.

Figure 9 displays the Pareto fronts obtained for each hyper-reduction method with respect to the combined state error and relative online wall time. In the reproductive scenario, EQP makes up the overall Pareto front across most error ranges, with the exception of regions near  $10^0$ , with similar performance for all methods, and the lowest error levels, where Q-DEIM and DEIM are Pareto optimal. On the overall Pareto front, the lowest state error, slightly above  $10^{-2}$ , is achieved by Q-DEIM at a relative online time of approximately  $7 \times 10^{-1}$ . In the predictive scenario, no single method consistently outperform the other ones. The lowest state error of approximately  $4 \times 10^{-1}$  at relative online time  $6 \times 10^{-1}$ , again achieved by Q-DEIM. In both scenarios at the lowest attained error level, the ROM's computational time savings are small compared to the FOM, indicating the need to consider a tradeoff based on the balance between accuracy and efficiency. This tradeoff is feasible in the reproductive case, with a lowest relative error of compared to about 1%. However, it might not be possible to sacrifice accuracy in the predictive scenario, where the lowest relative errors is nearly 40%, limiting the applicability of the hyper-reduction methods of this study to accelerate nonlinear elasticity dynamics.

### 5.3 Lagrangian hydrodynamics

We consider the hydrodynamics of a compressible fluid governed by the Euler equations in a Lagrangian reference frame. Similarly to the nonlinear elasticity case, the medium is described as a function of time  $t$  and reference coordinates of the material particles  $\tilde{x} \in \tilde{\Omega} = \Omega(0)$  at initial time  $t = 0$ . In the Lagrangian description of the medium's motion, the physical quantities are expressed as a function of its initial position  $\tilde{x}$  and time  $t$ . The system of the Euler equations of compressible fluid dynamics in a Lagrangian reference frame is written as follows [71]

$$\begin{aligned}
\text{momentum conservation : } & \rho \frac{dv}{dt} = \nabla \cdot \sigma \\
\text{mass conservation : } & \frac{1}{\rho} \frac{d\rho}{dt} = -\nabla \cdot v \\
\text{energy conservation : } & \rho \frac{de}{dt} = \sigma : \nabla v \\
\text{equation of motion : } & \frac{dx}{dt} = v
\end{aligned} \tag{27}$$

where  $d/dt$  denotes the material derivative,  $\rho$  the density of the fluid,  $x$  and  $v$  the position and velocity of the particles,  $e$  the internal energy per unit mass and  $\sigma$  the deformation stress tensor. In the equations, the spatial differential operators act with respect to the current coordinates  $x$ . We consider an isotropic stress tensor  $\sigma = -pI + \sigma_a$  where  $p$  denotes the thermodynamic pressure and  $\sigma_a$  the artificial viscosity stress, both of which depend on the state variables nonlinearly. The thermodynamic pressure is described by the equation of state and can be expressed as a function of the density and internal energy. In what follows, we focus on the case of polytropic ideal gas with an adiabatic index  $\gamma > 1$ , which yields the equation of state

$$p = (\gamma - 1)\rho e. \tag{28}$$

The system is prescribed with an initial condition and a boundary condition  $n \cdot v = h$ , where  $n$  is the outward normal unit vector on the domain boundary.

The semidiscrete Lagrangian formulation involves a computational mesh that deforms based on the fluid velocity. Using the Reynolds transport theorem [71], the mass conservation in (27) is satisfied by

$$\rho(\tilde{x}, t) = \frac{\rho(\tilde{x}, 0)}{|J(\tilde{x}, t)|} \tag{29}$$

where  $J = \nabla_{\tilde{x}} x$  denotes the Jacobian of the deformation gradient. Moreover, any integrals over the current domain  $\Omega(t)$  involve the transformation to the reference domain  $\tilde{\Omega}$  using the determinant of the transformation gradient  $|J|$ .

To write the remaining equations in (27) in the variational form (2) we define the following quantities. The state variable is  $y = (v, e, x)$  with state space  $\mathcal{Y} = [H^1(\tilde{\Omega})]^d \times L^2(\tilde{\Omega}) \times [H^1(\tilde{\Omega})]^d$ . There is no algebraic variable  $z$ . We define the Hilbert

space  $\mathcal{H} = [L^2(\tilde{\Omega})]^d \times L^2(\tilde{\Omega}) \times [L^2(\tilde{\Omega})]^d$  with inner product  $(\cdot, \cdot)_{\mathcal{H}}: \mathcal{H} \times \mathcal{H} \rightarrow \mathbb{R}$

$$((v, e, x), (v', e', x'))_{\mathcal{H}} = \int_{\Omega(t)} \rho v v' + \rho e e' + x x' dx$$

and denote by  $\mathcal{Y}'$  its dual with respect to  $(\cdot, \cdot)_{\mathcal{H}}$ . The bilinear form  $a: \mathcal{Y} \times \mathcal{Y} \rightarrow \mathbb{R}$  is given by

$$a((v, e, x), (v', e', x')) = - \int_{\Omega(t)} v x' dx$$

while the action of the nonlinear function  $f: \mathcal{Y} \times (0, T) \rightarrow \mathcal{Y}'$  by

$$\langle f(v, e, x, t), (v', e', x') \rangle_{\mathcal{Y}' \times \mathcal{Y}} = \int_{\Omega(t)} -\sigma(v, e, x) : \nabla v' + (\sigma(v, e, x) : \nabla v) e' dx.$$

Following [58] we adopt a spatial discretization for (27) using a kinematic space  $\mathcal{V}_V^h \subset [H^1(\tilde{\Omega})]^d$  for approximating the position and velocity functions, and a thermodynamic space  $\mathcal{V}_E^h \subset L_2(\tilde{\Omega})$  for approximating the energy. The density can be eliminated, and the equation of mass conservation can be decoupled from (27). We assume a high order finite element discretization in space, so that the finite dimensions  $N_V$  and  $N_E$  are the global numbers of FEM degrees of freedom (DOFs) in the corresponding discrete FEM spaces. The FEM coefficient vector functions for velocity, position and energy are respectively denote by  $\mathbf{v}: (0, T] \rightarrow \mathbb{R}^{N_V}$ ,  $\mathbf{x}: (0, T] \rightarrow \mathbb{R}^{N_V}$  and  $\mathbf{e}: \times (0, T] \rightarrow \mathbb{R}^{N_E}$ . The semidiscrete Lagrangian conservation laws can then be expressed as a nonlinear system of differential equations with size  $N_y = 2N_V + N_E$ . We refer the reader to [58] for additional details on the resulting semidiscrete equations.

We perform numerical simulations of three problem cases: Sedov blast, Taylor-Green vortex and triple point, introduced in the following sections. For each problem we focus on reproductive simulations, where the constructed reduced models are tested using initial conditions that were part of their training data.

Each problem case is time integrated using two methods: the 4-stage Runge Kutta (RK4) method displaying convergence for higher-order time integration, and the averaged 2-stage Runge Kutta (RK2Avg) method commonly used in real world applications [58, 72]. We employ the time windowing technique, where the simulation time interval is decomposed into a number of time sub-intervals (windows), with a temporally-local reduced model constructed for each window. The number of time windows used is determined by prescribing the number of FOM solution snapshots to be collected per window. For each problem, the number of snapshots and residual energy fraction  $E_r$  are such as to ensure an adequate basis size for each window. Finally, we also employ an adaptive timestepping strategy to dynamically adjust the timesteps during each simulation [26, 58].

The parameters used for the reduced simulations of each problem are summarized in Table 2, including the prescribed number of snapshots per window (# samples), the number of time windows (# windows) and reduced basis dimensions ( $r_v$  and  $r_e$ ). A detailed development of the reduction process using interpolation hyper-reduction methods is given in [26] and using quadrature methods in [28].

**Table 2:** Parameters used for the reduced simulations of Lagrangian hydrodynamics problems.

Problem	$E_r$	ODE solver	# sample	# windows	$r_v$	$r_e$
Sedov blast	6	RK2Avg	50	15	151	40
		RK4	100	15	118	37
Taylor-Green	6	RK2Avg	300	2	8	23
		RK4	600	2	8	22
Triple point	6	RK2Avg	100	2	12	10
		RK4	200	2	11	10

### 5.3.1 Sedov blast

The Sedov blast problem is a three dimensional standard shock hydrodynamic test, involving the release of energy from a localized source and the formation of a propagating shock wave [73]. We consider a localized source of internal energy initially deposited at the origin of a three dimensional cube, in analogy to the two-dimensional test in [58]. The computational domain is the unit cube  $\hat{\Omega} = [0, 1]^3$  with wall boundary conditions on all surfaces,  $v \cdot n = 0$ . We prescribe initial velocity  $v = 0$  and initial density  $\rho = 1$ . The initial energy is given by a delta function supported at the origin. In our implementation, the delta function energy source is approximated by setting the internal energy to zero in all degrees of freedom except at the origin, with  $e(0, 0, 0) = 0.25$ . The adiabatic index in the ideal gas equation of state is set to  $\gamma = 1.4$ .

Figure 10 illustrates the performance of the constructed reduced models with respect to the number of sampled interpolation/quadrature points, averaged over the number of time windows, across different hyper-reduction methods. Our comparisons focus on the achieved ROM performance between the two ODE solvers (RK4 and RK2Avg) under a fixed residual energy fraction  $E_r$  as given in Table 2. To obtain the presented results we increase the number of sampled interpolation points for interpolation methods and the number of nonzero sparse quadrature weights for EQP within each time window. The figure compares the performance for each of the three state variables: position, velocity and energy. The position field generally exhibits the smallest error, while the ordering of the energy and velocity errors depends on the case. For both solvers, the EQP method is the most efficient in terms of the number of quadrature points, achieving a given error level with approximately one order of magnitude fewer quadrature points. For the RK4 solver, EQP attains lower errors than the interpolation methods for the position and velocity fields; however, for the energy field, EQP does not achieve the lowest error levels, with the best interpolation results being nearly one order of magnitude smaller. Among the interpolation methods, DEIM generally demonstrates the most efficient performance in terms of the number of sampled interpolation points. For the RK2Avg solver, the interpolation methods achieve lower errors than EQP across all fields considered. Among them, S-OPT shows a slight advantage for the velocity field at lower error levels, whereas the position and energy fields exhibit comparable performance.

Comparing the two solvers, EQP shows little difference in error between RK4 and RK2Avg, with RK4 yielding slightly smaller errors for the velocity and energy fields.

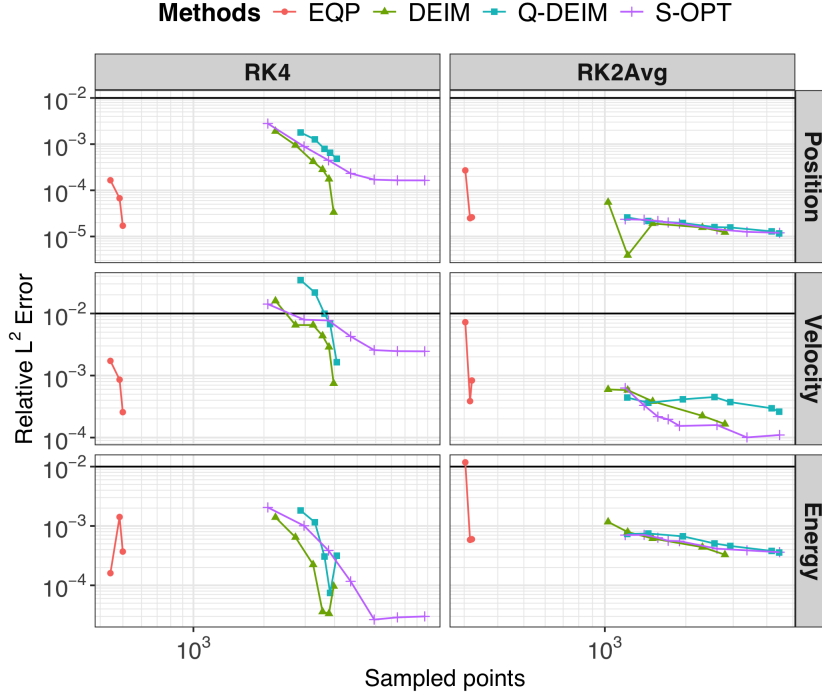


**Fig. 10:** ROM performance comparison for the Sedov blast wave problem with varying number of interpolation/quadrature points.

In contrast, the interpolation methods exhibit more pronounced solver dependence. For the velocity and position fields, RK2Avg enables an improvement of approximately one order of magnitude in the attainable error, reaching error levels of approximately  $10^{-5}$  for the position field and  $10^{-4}$  for the velocity field. For the energy field, however, RK2Avg results in errors that are roughly one order of magnitude larger than those obtained with RK4, with minimum errors around  $3 \times 10^{-4}$ . Overall, while EQP is highly efficient in terms of the number of sampled points, the achievable error levels across methods vary with the solver and state component.

Figure 11 reveals the tradeoff between approximation accuracy and time, showing the Pareto fronts for  $L^2$ -product norm of the error in the state  $(v, e, x)$ , for each method and solver. For the RK4 solver, the EQP method dominates the overall Pareto front at error levels below  $2 \times 10^{-3}$ , with a relative online time of approximately  $6 \times 10^{-2}$ . Among the interpolation methods, DEIM achieves the best performance and occupies the upper segment of the overall Pareto front, reaching its lowest error level near  $8 \times 10^{-4}$  at a relative online time of about  $7 \times 10^{-2}$ . In the case of the RK2Avg solver, the interpolation methods constitute the Pareto-optimal set, with no single method dominating the others. The lowest velocity error is obtained by DEIM, achieving an error level of  $4 \times 10^{-4}$  at a relative online time of about  $5 \times 10^{-2}$ . Although the interpolation methods require considerably more sampled interpolation points than EQP,

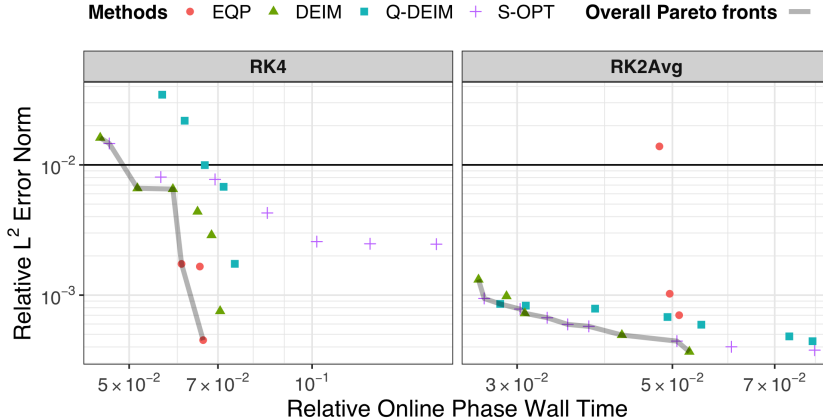


**Fig. 11:** Overall Pareto fronts across all hyper-reduction methods for the Sedov blast wave problem.

their relative online times are comparable or even smaller. This could be due to computational overhead stemming from the EQP sample mesh implementation, as discussed in the introduction of Section 5. We also note the solver dependent performance of each hyper-reduction method. For EQP, the error and relative online time are similar across solvers. For S-OPT, both solvers exhibit gradual tradeoffs: RK4 spans error levels between  $10^{-2}$  and  $10^{-3}$  over relative online times from  $4 \times 10^{-2}$  to  $2 \times 10^{-1}$ , whereas RK2Avg reaches lower error levels between  $10^{-3}$  and  $4 \times 10^{-4}$  at smaller relative online times from  $2 \times 10^{-2}$  to  $8 \times 10^{-2}$ . For DEIM and Q-DEIM, both methods exhibit a relatively steep tradeoff under RK4, with the error dropping from  $10^{-2}$  to  $10^{-3}$  over a narrower relative online time range of approximately  $4 \times 10^{-2}$  to  $7 \times 10^{-2}$ . Under RK2Avg, however, DEIM and Q-DEIM follow a more gradual tradeoff, similar to that observed for S-OPT. Overall, RK2Avg paired with interpolation methods yields the most favorable performance across the results considered.

### 5.3.2 Taylor-Green vortex

The Taylor-Green vortex problem is a three dimensional standard benchmark test for the incompressible inviscid Navier-Stokes equations. In this work we manufacture a smooth solution by extending the steady state Taylor-Green vortex solution to the compressible Euler equations, in analogy to the two-dimensional test in [58]. Our computation domain is the unit cube  $\tilde{\Omega} = [0, 1]^3$  with wall boundary conditions on all surfaces,  $v \cdot n = 0$ . Denoting  $\tilde{x} = (\tilde{x}_1, \tilde{x}_2, \tilde{x}_3) \in \tilde{\Omega}$ , the initial velocity is given by

$$v(\tilde{x}, 0) = (\sin(\pi\tilde{x}_1) \cos(\pi\tilde{x}_2) \cos(\pi\tilde{x}_3), -\cos(\pi\tilde{x}_1) \sin(\pi\tilde{x}_2) \cos(\pi\tilde{x}_3))$$

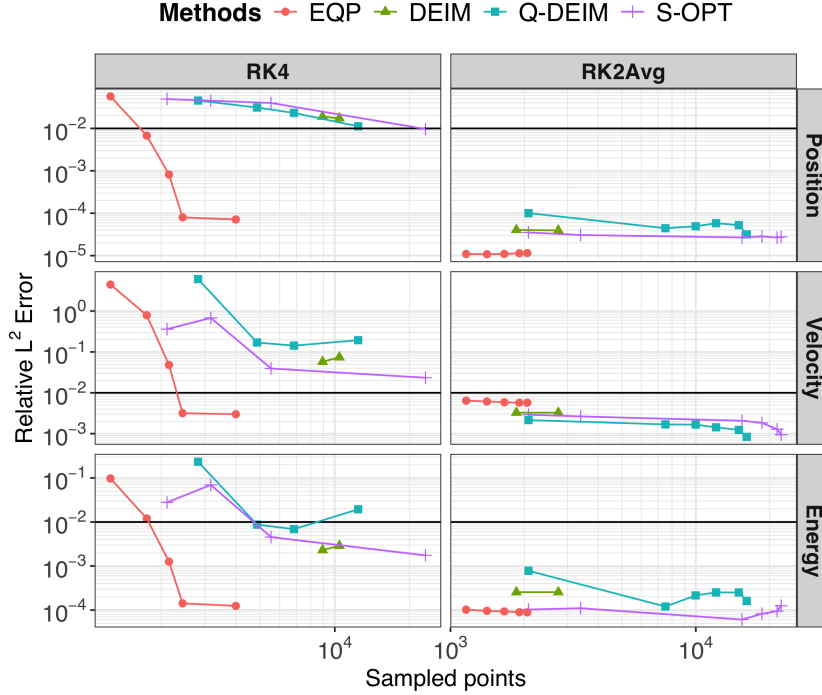


**Fig. 12:** ROM performance comparison for the Taylor-Green vortex problem with varying number of interpolation/quadrature points.

and the initial thermodynamic pressure by

$$p(\tilde{x}, 0) = 100 + \frac{(\cos(2\pi\tilde{x}_1) + \cos(2\pi\tilde{x}_2))(\cos(2\pi\tilde{x}_3) + 2) - 2}{16}$$

with initial density  $\rho = 1$ . Based on the above, the initial energy is determined by the equation of state (28) with adiabatic index set to  $\gamma = 5/3$ .

Figure 12 summarizes the ROM performance with respect to the average number of interpolation/quadrature points for the tested hyper-reduction methods. With the RK4 solver, the EQP method requires fewer quadrature points than the interpolation methods to reach a given error level across all variables. More specifically, EQP achieves roughly an order of magnitude lower velocity error than the interpolation methods while using fewer quadrature points. Among the interpolation methods, S-OPT tends to exhibit the most efficient performance in terms of the number of quadrature points required for a given velocity error. With the RK2Avg solver, however, a different trend is observed. Although EQP still requires fewer quadrature points, its velocity error levels remain higher than those of the interpolation methods. For approximately  $2 \times 10^3$  quadrature points, the interpolation methods achieve

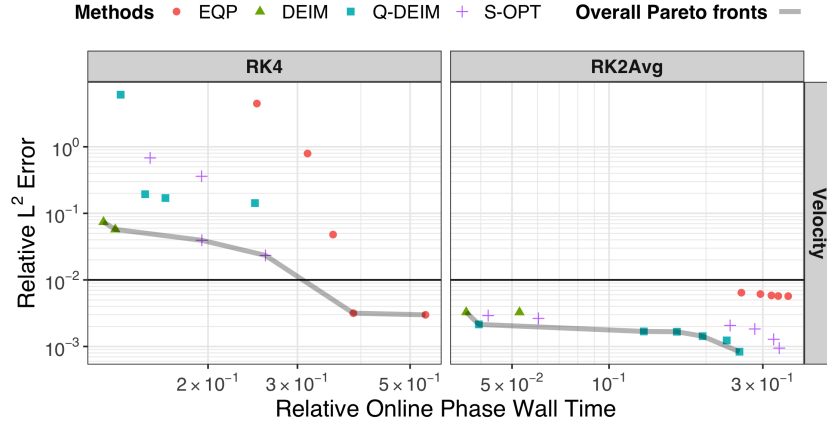


**Fig. 13:** Overall Pareto fronts across all hyper-reduction methods for the Taylor-Green vortex problem.

lower velocity errors than EQP. The minimum velocity error obtained with the interpolation methods is approximately one order of magnitude smaller than that of EQP, albeit with a larger number of sampled interpolation points. Overall, EQP demonstrates greater efficiency with the RK4 solver, whereas with RK2Avg the interpolation methods yield higher accuracy in velocity.

Figure 13 focuses on the tradeoff between computational time and  $L^2$ -product norm of the error in the state  $(v, e, x)$  across different hyper-reduction methods. With the RK4 solver, the Pareto-optimal configurations progress from DEIM to S-OPT and finally to EQP as the error level decreases. The lowest total error is achieved by EQP, reaching approximately  $3 \times 10^{-3}$  with a relative online time slightly below  $4 \times 10^{-1}$ . With RK2Avg the overall Pareto front is dominated by the interpolation methods. They attain a total error of about  $2 \times 10^{-3}$  at a relative online time of  $4 \times 10^{-2}$ , and around  $10^{-3}$  at  $2 \times 10^{-1}$ . Among them, Q-DEIM generally forms the Pareto front. To compare the performance of each method depending on the solver, all interpolation methods perform better with RK2Avg than with RK4. For EQP, the minimum obtained total error is slightly smaller with the RK4 solver, while the corresponding relative online times are of a similar magnitude. Overall, the interpolation methods exhibit shorter relative online times across both solvers. However, when using RK4 the lowest error is obtained by EQP at around  $3 \times 10^{-3}$ , making it the preferred option for accuracy below  $10^{-2}$ . The lowest total error among all configurations is attained by Q-DEIM with the RK2Avg solver, reaching the  $10^{-3}$  level.

### 5.3.3 Triple point

The triple point problem is a three dimensional hydrodynamic shock test that features two materials in three different states. More specifically, we consider a three state, two material, 2D Riemann problem which generates vorticity, analogous to the two dimensional test in [58]. The computational domain is  $\tilde{\Omega} = [0, 7] \times [0, 3] \times [0, 1.5]$

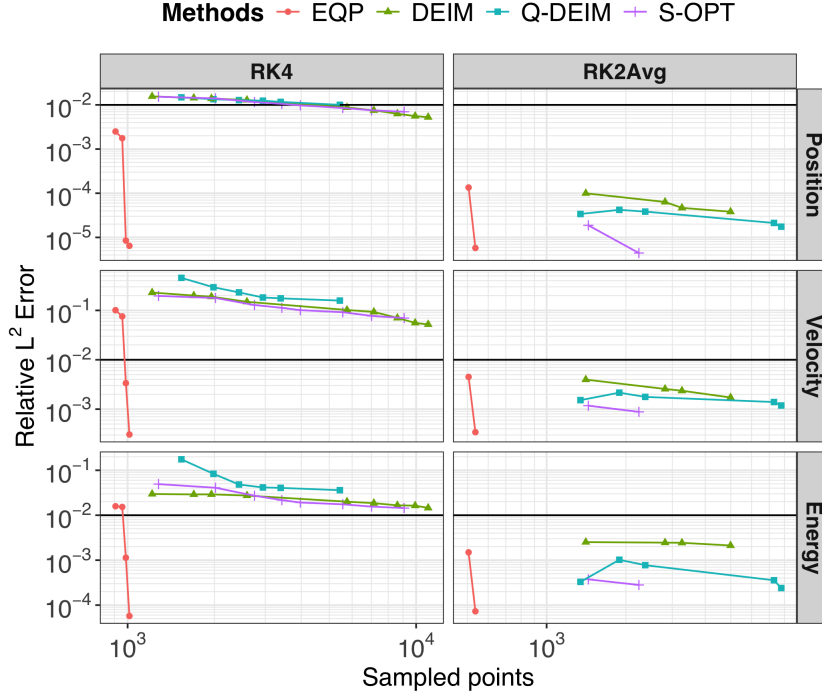


**Fig. 14:** ROM performance comparison for the triple point problem with varying number of interpolation/quadrature points.

with wall boundary conditions. The initial velocity is given by  $v = 0$ . Denoting  $\tilde{x} = (\tilde{x}_1, \tilde{x}_2, \tilde{x}_3) \in \tilde{\Omega}$ , the initial density is given by

$$\rho(\tilde{x}, 0) = \begin{cases} 1 & \text{if } \tilde{x}_1 \leq 1 \text{ or } \tilde{x}_2 \leq 1.5 \\ 1/8 & \text{if } \tilde{x}_1 > 1 \text{ and } \tilde{x}_2 > 1.5 \end{cases}$$

and the initial thermodynamic pressure by

$$p(\tilde{x}, 0) = \begin{cases} 1 & \text{if } \tilde{x}_1 \leq 1 \\ 1/8 & \text{if } \tilde{x}_1 > 1. \end{cases}$$

The adiabatic index is set to

$$\gamma(\tilde{x}, 0) = \begin{cases} 1.4 & \text{if } \tilde{x}_1 > 1 \text{ and } \tilde{x}_2 \leq 1.5 \\ 1.5 & \text{otherwise} \end{cases}$$

with the initial energy then determined by (28).

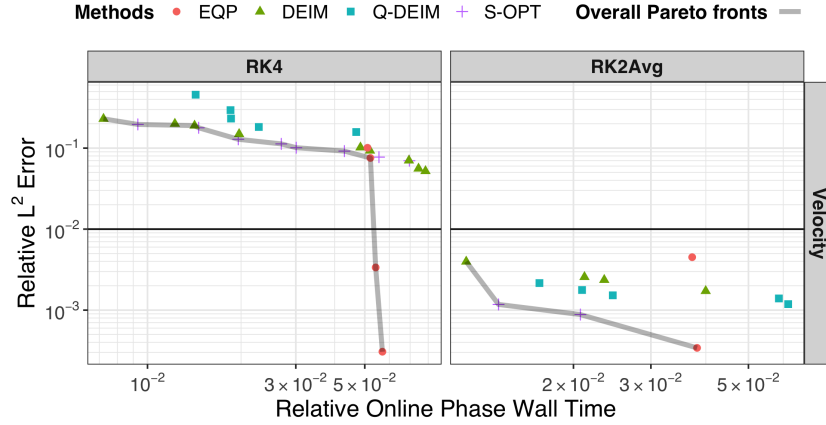


**Fig. 15:** Overall Pareto fronts across all hyper-reduction methods for the triple point problem.

Beginning with Figure 14 we see that EQP achieves a velocity error slightly above  $10^{-4}$  with both solvers. With RK4 this error is obtained with  $10^3$  quadrature points, while with RK2Avg a comparable error level is reached with roughly half as many quadrature points. Contrary to EQP, the performance of the interpolation methods varies significantly between the two solvers. With RK4 these methods are less efficient, exhibiting minimum velocity errors around  $5 \times 10^{-2}$ , more than two orders of magnitude larger than EQP. With RK2Avg their performance improves considerably, reaching minimum velocity errors of about  $10^{-3}$ , which represents a marked improvement over RK4, albeit still higher than EQP. The interpolation methods typically require between  $10^3$  and  $10^4$  sampled interpolation points, exceeding those required by EQP. Overall, EQP attains lower velocity errors using fewer quadrature points across both solvers.

Figure 15 shows that, although the interpolation methods use more sampled points than EQP, their relative online times are comparable or even smaller for the triple-point problem. As discussed in Section 5.3.1, this discrepancy between the number of quadrature points and relative online wall time could be due to differences in sample meshes between EQP and interpolation-based methods, see Figure 2. For both solvers, the Pareto optimal configurations are initially composed of interpolation methods, with EQP taking over for lower error levels. At the lowest error levels, EQP achieves total errors of approximately  $3 \times 10^{-4}$  with relative online times of about  $4 \times 10^{-2}$  for RK2Avg and  $6 \times 10^{-2}$  for RK4. On the contrary, the interpolation methods exhibit lower relative online times and reduced accuracy. With the RK4 solver they constitute the Pareto optimal set when the relative online time is below  $5 \times 10^{-2}$ , corresponding to total errors around  $10^{-1}$ . With RK2Avg they remain Pareto optimal when the relative online time is below  $3.5 \times 10^{-2}$ , with total errors of  $9 \times 10^{-3}$  or higher. Consistent with earlier observations, these methods perform significantly better with RK2Avg

than with RK4. Overall, EQP remains the most accurate method across both solvers, whereas interpolation methods offer a clear accuracy–efficiency tradeoff.

## 6 Conclusion

We introduced a variational framework for describing PDEs solved by hyper-reduced models. Five example problems were stated in terms of this framework and solved using four hyper-reduction methods: three gappy POD-based interpolation methods and the EQP quadrature method. We compared the relative performance of these hyper-reduction methods by computing the Pareto optimal front with respect to speed-up and accuracy.

For the nonlinear diffusion and elasticity problems, we considered two types of simulations: (1) reproductive, where the reduced model is tested for parameter values that were used in its training; (2) predictive, where the reduced model predicts solutions for parameter values not used during its training. In the Lagrangian hydrodynamics problems, we considered only reproductive simulations. Our numerical experiments demonstrate that the performance of the tested hyper-reduction methods depends on the problem and time integration method used, with no single method being universally superior.

In the diffusion problem, the EQP method was generally more efficient in terms of relative online time in the reproductive scenario, reaching similar error levels to the interpolation methods but with higher speed-up. In the predictive scenario, the differences among the methods were less pronounced, with EQP and interpolation methods displaying similar performance at lower error levels.

While the nonlinear elasticity problem exhibited higher errors than the other problems for the same energy fractions, a similar trend appeared: EQP was generally more efficient in the reproductive scenario and less dominant in the predictive one. The Q-DEIM method achieved the lowest errors across both scenarios, at the expense of a low relative speed-up of only 40%.

For the Lagrangian hydrodynamics problems, the performance of the interpolation methods was strongly influenced by the employed time integration method: interpolation methods performed consistently better with RK2Avg than with RK4. On the other hand, EQP did not demonstrate a clear dependency on the used time integration method.

For interpolation methods, each selected mesh element includes all associated interpolation points, whereas EQP selects quadrature points individually from the whole mesh. This can explain why EQP achieved higher efficiency with respect to the number of quadrature points in most of our numerical results. However, due to computational overhead in the creation of the sampled mesh elements, this advantage did not translate to the expected efficiency in relative online time in our Lagrangian hydrodynamics test cases.

Overall, our findings demonstrate that the EQP method can provide a significant speed-up at high accuracy levels for a broad range of problems. Nevertheless, interpolation methods can achieve a higher speed-up or better accuracy in certain cases. The relative performance of the studied hyper-reduction methods depends on the problem

case, choice of time integration method, and whether the tested simulation is reproductive or predictive. These results highlight the need for problem-specific selection of hyper-reduction strategies when choosing between interpolation and quadrature methods.

## Acknowledgments

This work was supported in part by the U.S. Department of Energy, Office of Science, Office of Advanced Scientific Computing Research, Scientific Discovery through Advanced Computing (SciDAC) program through the LEADS SciDAC Institute under Project Number SCW1933 at Lawrence Livermore National Laboratory (LLNL). LLNL is operated by Lawrence Livermore National Security LLC, for the U.S. Department of Energy, National Nuclear Security Administration under Contract DE-AC52-07NA27344. IM release number: LLNL-JRNL-2013738. Axel Larsson was supported by the U.S. National Science Foundation Grant award number 2122269. Part of this work was performed while Axel Larsson, Minji Kim and Chris Vales were research interns at LLNL supported by the Mathematical Sciences Graduate Internship (MSGI) program administered by the U.S. National Science Foundation. Chris Vales also acknowledges support from the U.S. Department of Energy under grant DE-SC0025101. The authors thank Adrian Humphry and Masayuki Yano from the University of Toronto for their valuable feedback on an earlier version of this manuscript and for providing a piece of the code used in our implementation of the empirical quadrature procedure.

## Disclaimer

This document was prepared as an account of work sponsored by an agency of the United States government. Neither the United States government nor Lawrence Livermore National Security LLC nor any of their employees makes any warranty, expressed or implied, or assumes any legal liability or responsibility for the accuracy, completeness, or usefulness of any information, apparatus, product, or process disclosed, or represents that its use would not infringe privately owned rights. Reference herein to any specific commercial product, process, or service by trade name, trademark, manufacturer, or otherwise does not necessarily constitute or imply its endorsement, recommendation, or favoring by the United States government or Lawrence Livermore National Security LLC. The views and opinions of authors expressed herein do not necessarily state or reflect those of the United States government or Lawrence Livermore National Security LLC and shall not be used for advertising or product endorsement purposes.

## A Command line options

To facilitate the reproduction of our results, we present the command line options used for each problem. Examples are provided for the predictive scenarios in Sections 5.1 and 5.2 and for the reproductive scenario with the RK2Avg solver in Section 5.3. Each

problem corresponds to a specific executable: `mixed_nonlinear_diffusion` in `libROM`, `nonlinear_elasticity_global_rom` in `libROM` and `laghos` in `Laghos`. Due to ongoing development in the repository, the presented commands are subject to change. The following commands are compatible with the recent commits of the `master` branch of MFEM <sup>1</sup>, the `master` branch of `libROM` <sup>2</sup>, and the `rom` branch of `Laghos` <sup>3</sup>. In order to use the ROM capability of `Laghos`, the user has to navigate to the `rom` subdirectory.

The conventions used in the examples are as follows. For Sections A.1 and A.2, the following apply to the online phase:

- EQP method: use the options `-eqp -ns`; the number of quadrature points can be restricted with `-maxnnls`.
- Interpolation methods: specify the hyper-reduction method via `-hrtype` and the number of sampling points with `-nsr`.

For Section A.3:

- `-s 7` corresponds to the RK2Avg solver and `-s 4` to RK4; RK2Avg is used in the examples.
- EQP method: requires the `-eqp` option in the merge phase; in the preprocessing and online phases use `-hrsamptype eqp` and `-lqnnls`.
- Interpolation methods: specify the hyper-reduction type in the preprocessing phase with `-hrsamptype`; the number of sampling points is controlled by `-sfacv` and `-sfacv`.

## A.1 Nonlinear diffusion

The following commands are used for the nonlinear diffusion problem in Section 5.1. The working directory is assumed to be `libROM/examples/prom`.

1. Offline phase (predictive scenario):

```
./mixed_nonlinear_diffusion -p 1 -offline -id 0 -sh 0.25
./mixed_nonlinear_diffusion -p 1 -offline -id 1 -sh 0.15
./mixed_nonlinear_diffusion -p 1 -offline -id 2 -sh 0.35
```

2. Merge phase:

```
./mixed_nonlinear_diffusion -p 1 -merge -ns 3
```

3. Create the FOM comparison data:

```
./mixed_nonlinear_diffusion -p 1 -offline -id 3 -sh 0.3
```

4. Online phase for EQP:

```
./mixed_nonlinear_diffusion -p 1 -online -rrdim 6 -rwdim 3 -id 3 -sh
0.3 -eqp -ns 3
```

Online phase for S-OPT:

```
./mixed_nonlinear_diffusion -p 1 -online -rrdim 6 -rwdim 3 -id 3 -sh
0.3 -nldim 6 -nsr 100 -hrtype sopt
```

---

<sup>1</sup>GitHub page, <https://github.com/mfem/mfem>, commit dc9128ef5

<sup>2</sup>GitHub page, <https://github.com/LLNL/libROM>, commit d8cc32c

<sup>3</sup>GitHub page, <https://github.com/CEED/Laghos/tree/rom>, commit ab24cfc

## A.2 Nonlinear elasticity

The following commands are used for the nonlinear diffusion problem in Section 5.2. The working directory is again assumed to be `libROM/examples/prom`.

1. Offline phase (predictive scenario):

```
./nonlinear_elasticity_global_rom -offline -dt 0.01 -tf 5.0 -s 14 -  
vs 100 -sc 0.9 -id 0  
./nonlinear_elasticity_global_rom -offline -dt 0.01 -tf 5.0 -s 14 -  
vs 100 -sc 1.1 -id 1
```

2. Merge phase:

```
./nonlinear_elasticity_global_rom -merge -ns 2 -dt 0.01 -tf 5.0
```

3. Create the FOM comparison data:

```
./nonlinear_elasticity_global_rom -offline -dt 0.01 -tf 5.0 -s 14 -  
vs 100 -sc 1.0 -id 2
```

4. Online phase for EQP:

```
./nonlinear_elasticity_global_rom -online -dt 0.01 -tf 5.0 -s 14 -vs  
100 -eqp -ns 2 -rvdim 3 -rxdim 2 -hdim 1 -sc 1.0
```

Online phase for S-OPT:

```
./nonlinear_elasticity_global_rom -online -dt 0.01 -tf 5.0 -s 14 -vs  
100 -hyp -hrtype sopt -rvdim 3 -rxdim 2 -hdim 5 -nsr 100 -sc  
1.0
```

## A.3 Lagrangian hydrodynamics

The following commands are used for the Lagrangian hydrodynamics simulations in Section 5.3. The working directory is assumed to be `Laghos/rom`

**Problem specification:** First, we present the commands used to set up each problem.

- Sedov blast problem:

```
./laghos -m data/cube01_hex.mesh -p 1 -pt 211 -s 7 -tf 0.2
```

- Taylor-Green problem:

```
./laghos -m data/cube01_hex.mesh -p 0 -cfl 0.1 -s 7 -tf 0.1
```

- Triple-point problem:

```
./laghos -m data/box01_hex.mesh -p 3 -cfl 0.5 -s 7 -tf 0.5
```

**ROM simulation:** Next, we present the command line options used in each stage of the ROM simulation for the Sedov blast problem. These options should be appended to the problem setup command for Sedov, except for the merge phase, which is executed independently. The same procedure applies to the other problems by replacing the problem specification accordingly. Below, we provide example commands for EQP and S-OPT.

1. Offline phase:
 

```
-offline -writesol -romsns -rpar 0 -rostype interpolate -sdim 10000
      -sample-stages
```
2. Merge phase for EQP (executed independently):
 

```
./merge -nset 1 -romsns -romos -rostype interpolate -nwinsamp 50 -ef
      0.999999 -eqp
```

 Merge phase for S-OPT (executed independently):
 

```
./merge -nset 1 -romsns -romos -rostype interpolate -nwinsamp 50 -ef
      0.999999
```
3. Hyper-reduction preprocessing phase for EQP:
 

```
-online -romhrprep -romsns -rostype interpolate -nwin 15 -hrsamptype
      eqp -lqnpls
```

 Hyper-reduction preprocessing phase for S-OPT:
 

```
-online -romhrprep -romsns -rostype interpolate -nwin 15 -hrsamptype
      sopt -sfacv 2 -sface 2
```
4. ROM online phase for EQP:
 

```
-online -romhr -romsns -rostype interpolate -nwin 15 -hrsamptype eqp
      -lqnpls
```

 ROM online phase for S-OPT:
 

```
-online -romhr -romsns -rostype interpolate -nwin 15 -sfacv 2 -sface
      2
```
5. Postprocessing phase (solution reconstruction and error evaluation):
 

```
-restore -romsns -rostype interpolate -nwin 15 -soldiff
```

## References

- [1] Tarantola, A.: Inverse Problem Theory and Methods for Model Parameter Estimation. SIAM, Philadelphia (2005)
- [2] Biegler, L.T., Ghattas, O., Heinkenschloss, M., Bloemen Waanders, B.: Large-scale pde-constrained optimization: an introduction. In: Large-scale PDE-constrained Optimization, pp. 3–13. Springer, Berlin (2003)
- [3] Biegler, L.T., Ghattas, O., Heinkenschloss, M., Keyes, D., Bloemen Waanders, B.: Real-time PDE-constrained Optimization. SIAM, Philadelphia (2007)
- [4] Gunzburger, M.D.: Perspectives in Flow Control and Optimization. SIAM, Philadelphia (2002)
- [5] Anirudh, R., Archibald, R., Asif, M.S., Becker, M.M., Benkadda, S., Bremer, P.-T., Budé, R.H., Chang, C.-S., Chen, L., Churchill, R., et al.: 2022 review of

data-driven plasma science. *IEEE Trans. Plasma Sci.* (2023)

- [6] Schmid, P.J.: Dynamic mode decomposition of numerical and experimental data. *J. Fluid Mech.* **656**, 5–28 (2010)
- [7] Brunton, S.L., Proctor, J.L., Kutz, J.N.: Discovering governing equations from data by sparse identification of nonlinear dynamical systems. *Proc. Natl. Acad. Sci. USA* **113**(15), 3932–3937 (2016)
- [8] Lagaris, I.E., Likas, A., Fotiadis, D.I.: Artificial neural networks for solving ordinary and partial differential equations. *IEEE Trans. Neural Networks* **9**(5), 987–1000 (1998) <https://doi.org/10.1109/72.712178>
- [9] Merwe, R., Leen, T.K., Lu, Z., Frolov, S., Baptista, A.M.: Fast neural network surrogates for very high dimensional physics-based models in computational oceanography. *Neural Networks* **20**(4), 462–478 (2007) <https://doi.org/10.1016/j.neunet.2007.04.023>
- [10] Karniadakis, G.E., Kevrekidis, I.G., Lu, L., Perdikaris, P., Wang, S., Yang, L.: Physics-informed machine learning. *Nat. Rev. Phys.* **3**(6), 422–440 (2021)
- [11] Raissi, M., Perdikaris, P., Karniadakis, G.E.: Physics-informed neural networks: a deep learning framework for solving forward and inverse problems involving nonlinear partial differential equations. *J. Comput. Phys.* **378**, 686–707 (2019)
- [12] Kovachki, N., Li, Z., Liu, B., Azizzadenesheli, K., Bhattacharya, K., Stuart, A., Anandkumar, A.: Neural operator: learning maps between function spaces with applications to PDEs. *J. Mach. Learn. Res.* **24**(89), 1–97 (2023)
- [13] Gugercin, S., Antoulas, A.C.: A survey of model reduction by balanced truncation and some new results. *Int. J. Control* **77**(8), 748–766 (2004)
- [14] Benner, P., Gugercin, S., Willcox, K.: A survey of projection-based model reduction methods for parametric dynamical systems. *SIAM Rev.* **57**(4), 483–531 (2015)
- [15] Veroy, K., Prud’homme, C., Patera, A.T.: Reduced-basis approximation of the viscous burgers equation: rigorous a posteriori error bounds. *C.R. Math.* **337**(9), 619–624 (2003) <https://doi.org/10.1016/j.crma.2003.09.023>
- [16] Choi, Y., Carlberg, K.: Space–time least-squares Petrov–Galerkin projection for nonlinear model reduction. *SIAM J. Sci. Comput.* **41**(1), 26–58 (2019)
- [17] Choi, Y., Coombs, D., Anderson, R.: SNS: a solution-based nonlinear subspace method for time-dependent model order reduction. *SIAM J. Sci. Comput.* **42**(2), 1116–1146 (2020)

- [18] Carlberg, K., Choi, Y., Sargsyan, S.: Conservative model reduction for finite-volume models. *J. Comput. Phys.* **371**, 280–314 (2018)
- [19] Xiao, D., Fang, F., Buchan, A.G., Pain, C.C., Navon, I.M., Du, J., Hu, G.: Non-linear model reduction for the Navier–Stokes equations using residual DEIM method. *J. Comput. Phys.* **263**, 1–18 (2014)
- [20] Burkardt, J., Gunzburger, M., Lee, H.-C.: POD and CVT-based reduced-order modeling of Navier–Stokes flows. *Comput. Methods Appl. Mech. Eng.* **196**(1-3), 337–355 (2006)
- [21] Hoang, C., Choi, Y., Carlberg, K.: Domain-decomposition least-squares Petrov-Galerkin (DD-LSPG) nonlinear model reduction. *Comput. Methods Appl. Mech. Eng.* **384**, 113997 (2021)
- [22] Fritzen, F., Haasdonk, B., Ryckelynck, D., Schöps, S.: An algorithmic comparison of the hyper-reduction and the discrete empirical interpolation method for a nonlinear thermal problem. *Math. Comput. Appl.* **23**(1), 8 (2018)
- [23] Mojjani, R., Balajewicz, M.: Lagrangian basis method for dimensionality reduction of convection dominated nonlinear flows. arXiv:1701.04343 (2017)
- [24] Zhao, P., Liu, C., Feng, X.: POD-DEIM based model order reduction for the spherical shallow water equations with Turkel-Zwas finite difference discretization. *J. Appl. Math.* (2014)
- [25] Stefanescu, R., Navon, I.M.: POD/DEIM nonlinear model order reduction of an ADI implicit shallow water equations model. *J. Comput. Phys.* **237**, 95–114 (2013)
- [26] Copeland, D.M., Cheung, S.W., Huynh, K., Choi, Y.: Reduced order models for Lagrangian hydrodynamics. *Comput. Methods Appl. Mech. Eng.* **388**, 114259 (2022) <https://doi.org/10.1016/j.cma.2021.114259>
- [27] Cheung, S.W., Choi, Y., Copeland, D.M., Huynh, K.: Local Lagrangian reduced-order modeling for the Rayleigh-Taylor instability by solution manifold decomposition. *J. Comput. Phys.* **472**, 11655 (2023) <https://doi.org/10.1016/j.jcp.2022.111655>
- [28] Vales, C., Cheung, S.W., Copeland, D.M., Choi, Y.: Machine-precision energy conservative reduced models for Lagrangian hydrodynamics by quadrature methods. arXiv:2508.21279 (2025) <https://doi.org/10.48550/arXiv.2508.21279>
- [29] Glas, S., Patera, A.T., Urban, K.: A reduced basis method for the wave equation. *Int. J. Comput. Fluid Dyn.* **34**(2), 139–146 (2020)

- [30] Cheung, S.W., Chung, E.T., Efendiev, Y., Leung, W.T.: Explicit and energy-conserving constraint energy minimizing generalized multiscale discontinuous Galerkin method for wave propagation in heterogeneous media. *Multiscale Model. Simul.* **19**(4), 1736–1759 (2021)
- [31] Choi, Y., Brown, P., Arrighi, B., Anderson, R., Huynh, K.: Space-time reduced order model for large-scale linear dynamical systems with application to Boltzmann transport problems. *J. Comput. Phys.* **424**, 109845 (2021)
- [32] Cheng, M.-C.: A reduced-order representation of the Schrödinger equation. *AIP Adv.* **6**(9), 095121 (2016)
- [33] McBane, S., Choi, Y.: Component-wise reduced order model lattice-type structure design. *Comput. Methods Appl. Mech. Eng.* **381**, 113813 (2021)
- [34] Choi, Y., Boncoraglio, G., Anderson, S., Amsallem, D., Farhat, C.: Gradient-based constrained optimization using a database of linear reduced-order models. *J. Comput. Phys.* **423**, 109787 (2020)
- [35] Choi, Y., Oxberry, G., White, D., Kirchdoerfer, T.: Accelerating design optimization using reduced order models. *arXiv:1909.11320* (2019)
- [36] Jiang, R., Durlofsky, L.J.: Implementation and detailed assessment of a GNAT reduced-order model for subsurface flow simulation. *J. Comput. Phys.* **379**, 192–213 (2019)
- [37] Yang, Y., Ghasemi, M., Gildin, E., Efendiev, Y., Calo, V., *et al.*: Fast multiscale reservoir simulations with POD-DEIM model reduction. *SPE Journal* **21**(06), 2–141 (2016)
- [38] Wang, M., Cheung, S.W., Chung, E.T., Vasilyeva, M., Wang, Y.: Generalized multiscale multicontinuum model for fractured vuggy carbonate reservoirs. *J. Comput. Appl. Math.* **366**, 112370 (2020)
- [39] Amsallem, D., Zahr, M., Choi, Y., Farhat, C.: Design optimization using hyper-reduced-order models. *Struct. Multidiscip. Optim.* **51**(4), 919–940 (2015)
- [40] Grimberg, S., Farhat, C., Tezaur, R., Bou-Mosleh, C.: Mesh sampling and weighting for the hyperreduction of nonlinear Petrov-Galerkin reduced-order models with local reduced-order bases. *Int. J. Numer. Methods Eng.* **122**(7), 1846–1874 (2021)
- [41] Everson, R., Sirovich, L.: Karhunen–Loève procedure for gappy data. *J. Opt. Soc. Am. A* **12**(8), 1657–1664 (1995)
- [42] Barrault, M., Maday, Y., Nguyen, N.C., Patera, A.T.: An ‘empirical interpolation’ method: application to efficient reduced-basis discretization of partial differential

- equations. *C.R. Math.* **339**(9), 667–672 (2004) <https://doi.org/10.1016/j.crma.2004.08.006>
- [43] Chaturantabut, S., Sorensen, D.C.: Nonlinear model reduction via discrete empirical interpolation. *SIAM J. Sci. Comput.* **32**(5), 2737–2764 (2010)
- [44] Carlberg, K., Farhat, C., Cortial, J., Amsallem, D.: The GNAT method for nonlinear model reduction: Effective implementation and application to computational fluid dynamics and turbulent flows. *J. Comput. Phys.* **242**, 623–647 (2013)
- [45] Drmac, Z., Gugercin, S.: A new selection operator for the discrete empirical interpolation method—improved a priori error bound and extensions. *SIAM J. Sci. Comput.* **38**(2), 631–648 (2016)
- [46] Drmac, Z., Saibaba, A.K.: The discrete empirical interpolation method: canonical structure and formulation in weighted inner product spaces. *SIAM J. Matrix Anal. Appl.* **39**(3), 1152–1180 (2018)
- [47] Lauzon, J.T., Cheung, S.W., Shin, Y., Choi, Y., Copeland, D.M., Huynh, K.: S-OPT: a points selection algorithm for hyper-reduction in reduced order models. *SIAM J. Sci. Comput.* **46**(4), 474–501 (2024)
- [48] An, S.S., Kim, T., James, D.L.: Optimizing cubature for efficient integration of subspace deformations. *ACM Trans. Graph.* **27**(5), 1–10 (2008) <https://doi.org/10.1145/1409060.1409118>
- [49] Farhat, C., Chapman, T., Avery, P.: Structure-preserving, stability, and accuracy properties of the energy-conserving sampling and weighting method for the hyper reduction of nonlinear finite element dynamic models. *Int. J. Numer. Methods Eng.* **102**(5), 1077–1110 (2015)
- [50] Hernandez, J.A., Caicedo, M.A., Ferrer, A.: Dimensional hyper-reduction of nonlinear finite element models via empirical cubature. *Comput. Methods Appl. Mech. Eng.* **313**, 687–722 (2017)
- [51] Patera, A.T., Yano, M.: An LP empirical quadrature procedure for parametrized functions. *C.R. Math.* **355**(11), 1161–1167 (2017) <https://doi.org/10.1016/j.crma.2017.10.020>
- [52] Yano, M., Patera, A.T.: An LP empirical quadrature procedure for reduced basis treatment of parametrized nonlinear PDEs. *Comput. Methods Appl. Mech. Eng.* **344**, 1104–1123 (2019) <https://doi.org/10.1016/j.cma.2018.02.028>
- [53] Bhattacharyya, S., Tao, J., Gildin, E., Ragusa, J.C.: Hyper-reduction techniques for efficient simulation of large-scale engineering systems. *Arch. Comput. Methods Eng.*, 1–43 (2025)

- [54] Brands, B., Davydov, D., Mergheim, J., Steinmann, P.: Reduced-order modelling and homogenisation in magneto-mechanics: a numerical comparison of established hyper-reduction methods. *Math. Comput. Appl.* **24**(1), 20 (2019)
- [55] Delagnes, T., Henneron, T., Clenet, S., Fratila, M., Ducreux, J.: Comparison of hyper-reduction methods combined with pod: Model order reduction of a squirrel cage induction machine in nonlinear case. *IEEE Trans. Magn.* **60**(6), 1–10 (2024)
- [56] Romor, F., Stabile, G., Rozza, G.: Explicable hyper-reduced order models on nonlinearly approximated solution manifolds of compressible and incompressible navier-stokes equations. *J. Comput. Phys.* **524**, 113729 (2025)
- [57] Choi, Y., Arrighi, W.J., Copeland, D.M., Anderson, R.W., Oxberry, G.M., USDOE NNSA: libROM (2019). <https://www.osti.gov/servlets/purl/1505575>
- [58] Dobrev, V.A., Kolev, T.V., Rieben, R.N.: High-order curvilinear finite element methods for Lagrangian hydrodynamics. *SIAM J. Sci. Comput.* **34**(5), 606–641 (2012)
- [59] MFEM: Modular Finite Element Methods. [mfem.org. https://doi.org/10.11578/dc.20171025.1248](https://doi.org/10.11578/dc.20171025.1248)
- [60] Carlberg, K., Bou-Mosleh, C., Farhat, C.: Efficient non-linear model reduction via a least-squares Petrov-Galerkin projection and compressive tensor approximations. *Int. J. Numer. Methods Eng.* **86**, 155–181 (2011)
- [61] Peherstorfer, B., Drmac, Z., Gugercin, S.: Stability of discrete empirical interpolation and gappy proper orthogonal decomposition with randomized and deterministic sampling points. *SIAM J. Sci. Comput.* **42**(5), 2837–2864 (2020)
- [62] Pukelsheim, F.: *Optimal Design of Experiments*. SIAM, Philadelphia (2006)
- [63] Shin, Y., Xiu, D.: On a near optimal sampling strategy for least squares polynomial regression. *J. Comput. Phys.* **326**, 931–946 (2016)
- [64] Du, E., Yano, M.: Efficient hyperreduction of high-order discontinuous Galerkin methods: element-wise and point-wise reduced quadrature formulations. *J. Comput. Phys.* **466**, 111399 (2022) <https://doi.org/10.1016/j.jcp.2022.111399>
- [65] Sleeman, M.K., Yano, M.: Goal-oriented model reduction for parametrized time-dependent nonlinear partial differential equations. *Comput. Methods Appl. Mech. Eng.* **388**, 114206 (2022) <https://doi.org/10.1016/j.cma.2021.114206>
- [66] Lawson, C.L., Hanson, R.J.: *Solving Least Squares Problems*. SIAM, Philadelphia (1995)
- [67] Humphry, A., Yano, M.: Efficient hyperreduction for large-scale problems: exploiting reducible constraint manifolds in empirical quadrature procedure. *Int. J.*

- Numer. Meth. Eng. **126**(23), 70204 (2025) <https://doi.org/10.1002/nme.70204>
- [68] Aubry, N., Guyonnet, R., Lima, R.: Spatiotemporal analysis of complex signals: theory and applications. *J. Stat. Phys.* **64**, 683–739 (1991)
- [69] Chatterjee, A.: An introduction to the proper orthogonal decomposition. *Curr. Sci.* **78**(7), 808–817 (2000)
- [70] Hinze, M., Volkwein, S.: Proper orthogonal decomposition surrogate models for nonlinear dynamical systems: error estimates and suboptimal control. In: Benner, P., Sorensen, D.C., Mehrmann, V. (eds.) *Dimension Reduction of Large-scale Systems*, pp. 261–306. Springer, Berlin (2005)
- [71] Aris, R.: *Vectors, Tensors, and the Basic Equations of Fluid Mechanics*. Dover, New York (1989)
- [72] Sandu, A., Tomov, V., Cervena, L., Kolev, T.: Conservative high-order time integration for Lagrangian hydrodynamics. *SIAM J. Sci. Comput.* **43**(1), 221–241 (2021)
- [73] Sedov, L.I., Volkovets, A.: *Similarity and Dimensional Methods in Mechanics*. CRC Press, Boca Raton (2018)